Absorbing Quantization Error by Deformable Noise Scheduler for Diffusion Models

Mingrui Yang [*1 2] **Wei Huang** [*2] **Haonan Sheng** [*3] **Donglin Yang** [2] **Jichang Yang** [2] **Xin Yu** [2] **Huining Yu** [2]
Yuzhong Jiao [1 4] **Zhongrui Wang** [5 1] **Xiaojuan Qi** [2]

Figure 1. Our method offers a plug-and-play approach to improve the quantization performance of diffusion models (including Flow-matching), enabling seamless integration with existing PTQ methods without compromising inference speed.

Abstract

Diffusion models deliver state-of-the-art image quality but are expensive to deploy. Post-training quantization (PTQ) can shrink models and speed up inference, yet residual quantization errors distort the diffusion distribution (the timestep-wise marginal over $\boldsymbol{x}_t$), degrading sample quality. We propose a distribution-preserving framework that absorbs quantization error into the generative process without changing architecture or adding steps. Deformable Noise Scheduler (DNS) reinterprets quantization as a principled timestep shift, mapping the quantized prediction distribution $\boldsymbol{x}_t$ back onto the original diffusion distribution so that the target marginal is preserved. Unlike trajectory-preserving or noise-injection meth-

[*]Equal contribution [1]AI Chip Center for Emerging Smart Systems (ACCESS), Hong Kong, China [2]The University of Hong Kong, Hong Kong, China [3]City University of Hong Kong, Hong Kong, China [4]The Hong Kong University of Science and Technology, Hong Kong, China [5]Southern University of Science and Technology, Shenzhen, China. Correspondence to: Zhongrui Wang <wangzr@sustech.edu.cn>, Xiaojuan Qi <xjqi@eee.hku.hk>.

Proceedings of the 43rd International Conference on Machine Learning, Seoul, South Korea. PMLR 306, 2026. Copyright 2026 by the author(s).

ods limited to stochastic samplers, our approach preserves the distribution under both stochastic and deterministic samplers and extends to flow-matching with Gaussian conditional paths. It is plug-and-play and complements existing PTQ schemes. Empirically, our method consistently enhances generation quality across diverse backbones and existing PTQ baselines. Notably, when further quantizing the FP16 LoRA branch of SVDQuant to enable fully integer inference, our approach effectively mitigates the performance drop, reducing FID from 27.16 to 26.22. Code is available at DNS-AQE GitHub Repository.

1. Introduction

Diffusion models have become the leading paradigm for high-quality generative modeling, powering applications across image synthesis (Ho et al., 2020; Rombach et al., 2022; Labs, 2024), style transfer (Qi et al., 2024), video generation (Brooks et al., 2024), 3D reconstruction (Zhou et al., 2024), and robotics (Chi et al., 2024). Their rapid scaling– from Stable Diffusion's 800M parameters (Rombach et al., 2022) to SDXL's 2.6B (Podell et al., 2023), and most recently to FLUX.1's 12B (Labs, 2024)– has driven remarkable improvements in fidelity and controllability. However, these gains come at a steep computational cost: inference with large models demands tens of gigabytes of GPU memory and seconds per image, limiting deployment in real-time and resource-constrained settings.

Model quantization is a practical solution to this bottleneck. By reducing weights and activations from floating-point to low-bit integer, quantization compresses model size and accelerates inference (Jacob et al., 2017; Nagel et al., 2021). Recent post-training quantization (PTQ) methods have successfully reduced diffusion models to 8, 4 or even 1-bit precision (Li et al., 2023; Wu et al., 2024; Li et al., 2025); (Huang et al., 2024; Shang et al., 2023; Ye et al., 2024; Wang et al., 2024; Zheng et al., 2024). Yet, unlike discriminative networks or autoregressive language models, diffusion models are especially sensitive to quantization. Errors accumulate across iterative denoising steps, corrupting the assumed Gaussian noise distribution and significantly degrading sample quality (He et al., 2023).

Existing approaches attempt to mitigate this challenge by either reshaping weight distributions to reduce quantization error (Li et al., 2023; Wu et al., 2024; Li et al., 2025) or injecting approximated Gaussian noise to absorb residual errors (He et al., 2023). However, these methods have important limitations: weight-reshaping strategies only preserve stepwise predictions without addressing distributional drift, keeping sensitive branches in FP16 hinders deployment on integer-centric hardware, while noise-injection methods are restricted to stochastic samplers and fail on deterministic or flow-matching frameworks (Lipman et al., 2023). Moreover, quantization noise rarely follows an ideal Gaussian distribution, undermining the robustness of Gaussian-based corrections.

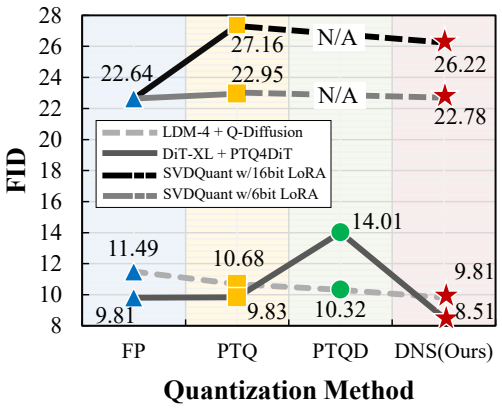

Figure 2. Comparison of FID scores across quantization methods for different backbones.

In this work, we introduce a distribution-preserving quantization framework that directly absorbs quantization error into the diffusion process. Our approach consists of two key components: (i) *Distribution-Calibrated Noise Compensation (DCNC)*: corrects the non-Gaussian kurtosis of quantization noise through a calibrated uniform component, yielding a more faithful Gaussian approximation. (ii) *Deformable Noise Scheduler (DNS)*: reinterprets quantization effects as a timestep shift in the diffusion process, aligning quantized prediction with the original diffusion distribution without modifying model architecture or adding inference overhead. This framework preserves the diffusion distribution under quantization, making it compatible with both stochastic and deterministic samplers as well as flow-matching models. It operates as a plug-and-play solution, easily integrated with existing PTQ methods. Empirically, our method consistently improves generation quality across diverse backbones (see Fig. 2). For example, on DiT-XL our method reduces the FID of PTQ4DiT (W4A8) from 9.83 to 8.51, surpassing even the FP16 baseline (9.81).

In summary, our contributions are threefold: (1) A principled analysis showing that quantization can be reinterpreted as timestep shifts in the diffusion process. (2) A deformable noise scheduler and distribution-calibrated correction that preserve the generative distribution under quantization. (3) Extensive experiments across LDM, DiT, and FLUX demonstrating consistent quality improvements without sacrificing the efficiency benefits of quantization.

2. Related Work

Diffusion Models. Diffusion models (Sohl-Dickstein et al., 2015; Ho et al., 2020) were originally formulated as stochastic processes for data generation. Denoising Diffusion Implicit Models (DDIM) (Song et al., 2022) later reduced the number of sampling steps, significantly accelerating the generation process. More recently, Flow Matching (Lipman et al., 2023) has been introduced as a deterministic alternative, powering state-of-the-art systems such as FLUX (Labs, 2024).

The backbone architecture of early diffusion models was primarily based on UNets (Rombach et al., 2022). Diffusion Transformers (DiT) (Peebles & Xie, 2023) pioneered the use of pure transformer architectures, leading to improved scalability and performance. Large-scale text-to-image models such as Stable Diffusion (Rombach et al., 2022), SDXL (Podell et al., 2023), PixArt (Chen et al., 2023), and FLUX (Labs, 2024) have since revolutionized content generation by pushing model sizes larger to achieve better fidelity, diversity, and controllability.

Model Quantization for Diffusion models. Quantization reduces computational costs by representing model parameters and activations with lower-precision formats. Approaches generally fall into two categories: quantization-aware training (QAT) (Jacob et al., 2017), which requires retraining with quantization in the loop, and post-training quantization (PTQ) (Nagel et al., 2021), which adapts pre-trained models with minimal calibration data. Due to the size and training cost of diffusion models, PTQ methods are more practical and thus widely adopted.

Specialized PTQ techniques have been developed to address the unique challenges of diffusion backbones. Q-Diffusion (Li et al., 2023) employs channel-wise quantization with explicit outlier handling. PTQ4DM (Shang et al., 2023) and PTQ4DiT (Wu et al., 2024) design quantization strategies tailored to their respective UNet and transformer backbones. MixDQ (Zhao et al., 2024) adopts mixed precision to balance efficiency and quality. SVDQuant (Li et al., 2025) introduces FP16 low-rank branches to capture residual information lost during quantization.

A different line of work, PTQD (He et al., 2023), proposes an "absorbing quantization error" strategy that integrates quantization noise into the random noise term of stochastic samplers. While effective in certain settings, this approach is fundamentally restricted to stochastic sampling and cannot be applied to deterministic samplers or flow-matching frameworks that dominate modern implementations. Moreover, the injected quantization noise often deviates from the expected Gaussian distribution, which can misalign the diffusion process and degrade generation quality.

3. Preliminary

3.1. Diffusion models and Flow matching

Diffusion Models (Ho et al., 2020; Song et al., 2022) are generative models based on a two-stage process: a fixed *forward* noising process and a learnable *reverse* denoising process.

In the forward process, a clean data sample $\boldsymbol{x}_0 \sim q(\boldsymbol{x}_0)$ is progressively corrupted by Gaussian noise over T timesteps via a Markov chain with a predefined variance schedule $\{\beta_t\}_{t=1}^T$, where $0 < \beta_t < 1$. Define $\alpha_t := 1 - \beta_t$ and $\bar{\alpha}_t := \prod_{i=1}^t \alpha_i$. The forward transition distributions are given by:

$$\begin{aligned} q(\boldsymbol{x}_t \mid \boldsymbol{x}_{t-1}) &= \mathcal{N}\big(\sqrt{\alpha_t}\,\boldsymbol{x}_{t-1},\, \beta_t \mathbf{I}\big), \\ q(\boldsymbol{x}_t \mid \boldsymbol{x}_0) &= \mathcal{N}\big(\sqrt{\bar{\alpha}_t}\,\boldsymbol{x}_0,\, (1-\bar{\alpha}_t)\mathbf{I}\big). \end{aligned} \tag{1}$$

The reverse process aims to recover $\boldsymbol{x}_0$ from $\boldsymbol{x}_T$ by learning a parametric approximation $p_\theta(\boldsymbol{x}_{t-1} \mid \boldsymbol{x}_t)$ to the true reverse distribution. Ho et al. (2020) (DDPM) model this reverse process as a Gaussian with fixed variance, trained to predict the noise added at each step. Song et al. (2022) (DDIM) generalize this by introducing a family of non-Markovian reverse processes parameterized by a noise schedule $\{\sigma_t\}_{t=1}^T$, enabling faster sampling with deterministic or stochastic trajectories.

Specifically, for any $t > 1$, the conditional distribution of $\boldsymbol{x}_{t-1}$ given $\boldsymbol{x}_t$ and clean sample $\boldsymbol{x}_0$ is:

$$q_\sigma(\boldsymbol{x}_{t-1} \mid \boldsymbol{x}_t, \boldsymbol{x}_0) = \mathcal{N}\big(\hat{\mu}_t(\boldsymbol{x}_t, \boldsymbol{x}_0),\, \sigma_t^2 \mathbf{I}\big)\,, \tag{2}$$

where $\sigma_t \geq 0$ controls the stochasticity of the reverse step and $\hat{\mu}_t(\boldsymbol{x}_t, \boldsymbol{x}_0) = \sqrt{\bar{\alpha}_{t-1}}\,\boldsymbol{x}_0 + \sqrt{1-\bar{\alpha}_{t-1}-\sigma_t^2} \cdot \frac{\boldsymbol{x}_t - \sqrt{\bar{\alpha}_t}\,\boldsymbol{x}_0}{\sqrt{1-\bar{\alpha}_t}}$. When $\sigma_t = \sqrt{(1-\bar{\alpha}_{t-1})/(1-\bar{\alpha}_t)} \cdot \sqrt{1-\bar{\alpha}_t/\bar{\alpha}_{t-1}}$, this recovers the DDPM posterior; when $\sigma_t = 0$, the process becomes deterministic (DDIM).

Since $\boldsymbol{x}_0$ is unknown during sampling, it is estimated from $\boldsymbol{x}_t$ using a noise-prediction network $\epsilon_\theta(\boldsymbol{x}_t, t)$. The denoised estimate $\hat{\boldsymbol{x}}_0$ is obtained via:

$$\hat{\boldsymbol{x}}_0 = \frac{1}{\sqrt{\bar{\alpha}_t}}\Big(\boldsymbol{x}_t - \sqrt{1-\bar{\alpha}_t}\,\varepsilon_\theta(\boldsymbol{x}_t, t)\Big). \tag{3}$$

The learned reverse process is then defined by substituting $\hat{\boldsymbol{x}}_0$ for $\boldsymbol{x}_0$ in Eq. 2:

$$p_\theta(\boldsymbol{x}_{t-1} \mid \boldsymbol{x}_t) = q_\sigma(\boldsymbol{x}_{t-1} \mid \boldsymbol{x}_t, \hat{\boldsymbol{x}}_0), \quad t > 1. \tag{4}$$

This leads to the unified sampling update rule:

$$\boldsymbol{x}_{t-1} = \sqrt{\bar{\alpha}_{t-1}}\,\hat{\boldsymbol{x}}_0 + \sqrt{1-\bar{\alpha}_{t-1}-\sigma_t^2}\;\frac{\boldsymbol{x}_t - \sqrt{\bar{\alpha}_t}\,\hat{\boldsymbol{x}}_0}{\sqrt{1-\bar{\alpha}_t}} + \sigma_t\, z \tag{5}$$

where $z \sim \mathcal{N}(0, \mathbf{I})$.

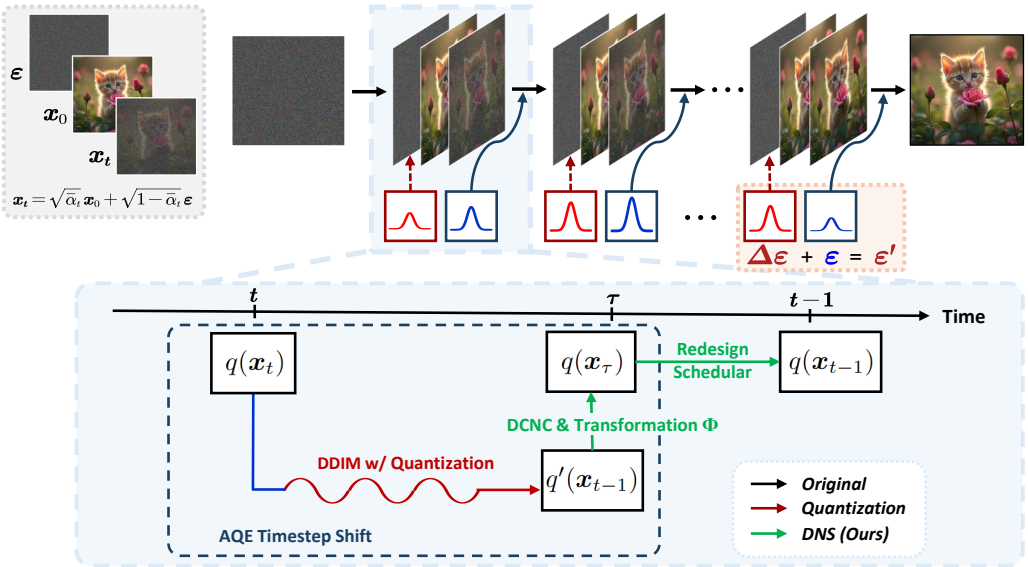

Figure 3. Overview of Deformable Noise Scheduler (DNS). (a) Top: Quantization perturbs the noise prediction (red), shifting each step's marginal away from the full-precision distribution (blue), yielding $\epsilon' = \epsilon + \Delta\epsilon$. These quantization errors are absorbed into the diffusion process, preserving the original prediction distribution. (b) Bottom: DNS interprets effect as *timestep shift*. The quantized distribution $q'(\boldsymbol{x}_{t-1})$ is mapped to original distribution $q(\boldsymbol{x}_\tau)$ via DCNC and transformation Φ. Redesigning scheduler sets a new α so that τ aligns with $t-1$, maintain original diffusion timesteps.

Flow matching (Lipman et al., 2023) generalizes diffusion via a continuous-time stochastic interpolant between Gaussian noise $\epsilon \sim \mathcal{N}(0, I)$ and data x_0. A simple linear interpolant is

$$\boldsymbol{x}_t = (1-t)\boldsymbol{x}_0 + t\epsilon, \quad t \in [0,1]. \tag{6}$$

The model learns a velocity field $\boldsymbol{v}_\theta(\boldsymbol{x}_t, t)$ such that the probability flow ODE (PF-ODE)

$$\frac{d\boldsymbol{x}_t}{dt} = \boldsymbol{v}_\theta(\boldsymbol{x}_t, t) \tag{7}$$

induces marginal distributions that match that of Eq. 6 for all time $t \in [0,1]$. Sampling from the model thus reduces to solving the PF-ODE in Eq. 7 using standard ODE solvers, e.g., Euler integration, starting from Gaussian noise $\boldsymbol{\varepsilon} \sim \mathcal{N}(0, \boldsymbol{I})$ (Lipman et al., 2023), which matches the ground-truth dynamics. Sampling then amounts to integrating this ODE deterministically from noise to data. Flow matching, owing to its high scalability, has already been adopted in modern text-to-image models such as FLUX (Labs, 2024). Flow matching thus unifies diffusion-style objectives with a deterministic transport formulation, and underlies modern large-scale systems such as FLUX (Labs, 2024).

3.2. Quantization Noise Correction and Absorption

Quantizing diffusion models inevitably introduces quantization error. This error can be systematically decomposed into two parts: (i) a correlated component that scales linearly with the original network output $\epsilon_\theta(\boldsymbol{x}_t, t)$, and (ii) an independent component $\Delta'\epsilon_\theta(\boldsymbol{x}_t, t)$ that is uncorrelated with the prediction. This decomposition, referred to as Correlation Noise Correction (CNC), can be written as:

$$\Delta\epsilon_\theta(\boldsymbol{x}_t, t) = k\epsilon_\theta(\boldsymbol{x}_t, t) + \Delta'\epsilon_\theta(\boldsymbol{x}_t, t) \tag{8}$$

where $\Delta\epsilon_\theta(\boldsymbol{x}_t, t)$ denotes total quantization error, k is a scalar correlation coefficient, and $\Delta'\epsilon_\theta(\boldsymbol{x}_t, t)$ represents the residual independent component. PTQD (He et al., 2023) approximates $\Delta'\epsilon_\theta(\boldsymbol{x}_t, t)$ as Gaussian noise, but in practice this assumption is often inaccurate. The variance of the independent noise, denoted σ_q^2, can instead be empirically estimated from representative data samples.

In stochastic sampling process, sampler involves adding random noise in Eq. 5. PTQD absorbs the disentangled independent quantization error into this random term, effectively replacing:

$$\sigma_t z \to \sigma_t z - \frac{\beta_t}{\sqrt{\alpha_t}\sqrt{1-\bar{\alpha}_t}(1+k)}\Delta'\epsilon_\theta(\boldsymbol{x}_t, t) \tag{9}$$

This leads to a modified update rule:

$$\begin{aligned}\boldsymbol{x}_{t-1} = \frac{1}{\sqrt{\alpha_t}}\left(\boldsymbol{x}_t - \frac{\beta_t}{\sqrt{1-\bar{\alpha}_t}}\epsilon_\theta(\boldsymbol{x}_t, t)\right) + \sigma_t z \\ - \frac{\beta_t}{\sqrt{\alpha_t}\sqrt{1-\bar{\alpha}_t}(1+k)}\Delta'\epsilon_\theta(\boldsymbol{x}_t, t)\end{aligned} \tag{10}$$

In summary, PTQD attempts to (i) preserve the injected noise distribution by treating the disentangled quantization

residual as Gaussian, while simultaneously (ii) preserving the stepwise prediction trajectory. However, this hybrid objective can degrade performance and reduce robustness, and it is applicable only to stochastic sampling. Moreover, empirical evidence shows that the independent quantization residual $\Delta'\epsilon_\theta$ has a large deviation from a Gaussian distribution. Directly using it may undermine the theoretical assumptions of the method.

4. Method

To address these limitations, we develop a theoretical framework that analyzes how quantization perturbs a diffusion model's predictive distribution and derives distribution-preserving corrections for both the noise statistics and the time parameterization. In Sec. 4.1, we show that the uncorrelated component of the quantization error is heavy-tailed (exhibits excess kurtosis relative to Gaussian noise) and mitigate this mismatch by adding a calibrated uniform correction with lower kurtosis. In Sec. 4.2, we prove that the distribution induced by a quantized model can be mapped to an equivalent non-quantized distribution through an appropriate timestep shift (Fig. 3), enabling the approach to be applied to any generative model with conditionally Gaussian marginals. A more detailed derivation is provided in Appendix A.2.

4.1. Gaussian Approximation of Quantization Noise

When the model is quantized, parameter perturbations introduce errors in the predicted noise. The output of the quantized model can be expressed as:

$$\epsilon'_\theta(\boldsymbol{x}_t, t) = \epsilon_\theta(\boldsymbol{x}_t, t) + \Delta\epsilon_\theta(\boldsymbol{x}_t, t) \tag{11}$$

where $\Delta\epsilon_\theta(\boldsymbol{x}_t, t)$ is a quantization-induced error.

Prior work (He et al., 2023) applied a disentangling transformation (Eq. 8) to separate $\Delta\epsilon_\theta(\boldsymbol{x}_t, t)$ into an "independent" component $\Delta'\epsilon_\theta(\boldsymbol{x}_t, t)$, which was then approximated as Gaussian noise and absorbed into the stochastic sampling term. However, our empirical analysis (see Fig. 4) shows that the residual noise obtained in this manner exhibits excess kurtosis relative to a true Gaussian distribution, violating this assumption.

To correct this, we introduce a refined transformation T such that

$$T(\epsilon'_\theta(\boldsymbol{x}_t, t)) = \epsilon_\theta(\boldsymbol{x}_t, t) + \Delta''\epsilon_\theta(0, \sigma_{\epsilon,t}) \tag{12}$$

where the independent component $\Delta''\epsilon_\theta(0, \sigma_{\epsilon,t})$ is explicitly calibrated to approximate a Gaussian distribution with mean 0 and variance $\sigma^2_{\epsilon,t}$ which depends on the timestep t. We refer to this procedure as *Distribution-Calibrated Noise Compensation* (DCNC). DCNC ensures that the residual quantization noise more faithfully matches the Gaussian assumption of the diffusion process, thereby improving stability and generation quality.

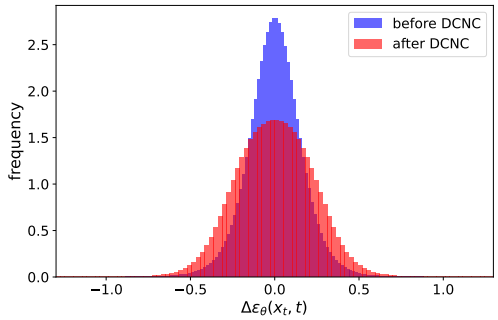

Figure 4. Quantization noise distribution before and after DCNC in timestep 250

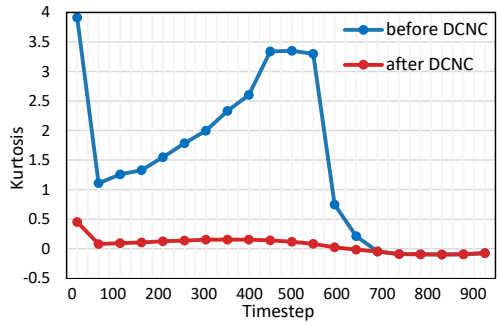

Figure 5. Kurtosis of quantization noise before and after DCNC

Distribution-Calibrated Noise Compensation To drive the excess kurtosis of the residual toward 0 (i.e., make it behave more like Gaussian noise), we add a zero-mean uniform component. Let the residual have variance σ_o^2 and excess kurtosis $\kappa_o > 0$. Then the variance of the injected uniform term and the resulting total variance are (derivation in Appendix A.1):

$$\sigma_u^2 = \sigma_o^2 \cdot \sqrt{5\kappa_o/6}\,, \qquad \sigma_n^2 = \sigma_o^2 \cdot \left(1 + \sqrt{5\kappa_o/6}\right) \tag{13}$$

As shown in Fig. 4 and Fig. 5, this uniform compensation substantially reduces the heavy-tailedness of the uncorrelated quantization residual, bringing its excess kurtosis close to the Gaussian value (0). More higher-order moments are also collected in Appendix.A.1 to demonstrate that residuals after DCNC are closer to a Gaussian. Accurate variance estimation is important for applying Eq. 13 and for the marginal analysis in Eq. 17. Because conventional estimators are sensitive to outliers, we use a robust IQR-based estimate $\hat{\sigma}^2 = (\mathrm{IQR}/1.349)^2$, where $\mathrm{IQR} = Q_3 - Q_1$ denotes the interquartile range, with Q_1 and Q_3 representing the first and third quartiles. Putting this together, our calibrated

transformation is:

$$T(\epsilon'_\theta(\boldsymbol{x}_t, t)) = \epsilon'_\theta(\boldsymbol{x}_t, t)/(1+k) + W_u \cdot U(0, \sigma_u^2) \quad (14)$$

where k (the correlation slope) and σ_u^2 are estimated during calibration, $U(0, \sigma_u^2)$ denotes a zero-mean uniform random variable with variance σ_u^2, and $W_u \in [0, 1]$ is a tunable weight that controls the strength of the correction (see Sec. 5.3). Unless stated otherwise, all model outputs are passed through $T(\cdot)$ before subsequent analysis and sampling.

4.2. Deformation of Sampling with Quantization Noise

After applying DCNC, the residual quantization error is well-approximated as zero-mean Gaussian. We leverage this property to *absorb* quantization effects into the diffusion process via a *timestep shift*: instead of introduced extra noise, we preserve distributional consistency via a timestep shift τ, aligning the quantized marginal distribution at t with the full-precision marginal distribution at τ. This distribution-preserving perspective removes the reliance on specific stochastic samplers. Our approach preserves the distribution under both stochastic and deterministic samplers and extends to flow matching with Gaussian conditional paths.

Absorbing Quantization Error by Timestep Shift In diffusion models, the reverse process $p_\theta(\boldsymbol{x}_{t-1} \mid \boldsymbol{x}_t)$ reconstructs $\boldsymbol{x}_{t-1}$ from the noisy sample $\boldsymbol{x}_t$ by leveraging an estimate $\hat{\boldsymbol{x}}_0$ of the clean data $\boldsymbol{x}_0$, as formalized in Eq. 4. When the model is quantized, the prediction $\hat{\boldsymbol{x}}_0$ is perturbed by quantization noise (Eq. 11), after correction (Eq. 12), yielding a modified estimate $\hat{\boldsymbol{x}}'_0$. Consequently, the reverse process distribution under quantization becomes:

$$\begin{aligned} p'_\theta(\boldsymbol{x}_{t-1} \mid \boldsymbol{x}_t) &= q_\sigma(\boldsymbol{x}_{t-1} \mid \boldsymbol{x}_t, \hat{\boldsymbol{x}}'_0) \\ &= \mathcal{N}\big(\boldsymbol{x}_{t-1};\, \hat{\mu}_t(\boldsymbol{x}_t, \hat{\boldsymbol{x}}_0),\, (\sigma_t^2 + C_1^2\sigma_{\epsilon,t}^2)\mathbf{I}\big), \end{aligned} \quad (15)$$

where

$$C_1 = \sqrt{\bar{\alpha}_{t-1}} - \sqrt{\frac{(1-\bar{\alpha}_{t-1}-\sigma_t^2)\bar{\alpha}_t}{1-\bar{\alpha}_t}}, \quad (16)$$

and $\sigma_{\epsilon,t}^2$ denotes the variance of the independent quantization residual at timestep t. Notably, quantization noise does not alter the mean of the reverse distribution but inflates its variance by an additive term $C_1^2\sigma_{\epsilon,t}^2$, reflecting the uncertainty introduced by model quantization.

Thus the induced conditional marginal distribution under quantization is

$$q'(\boldsymbol{x}_{t-1}|\boldsymbol{x}_0) = \mathcal{N}\big(\boldsymbol{x}_{t-1};\, \sqrt{\bar{\alpha}_{t-1}}\,\boldsymbol{x}_0, (1-\bar{\alpha}_{t-1}+C_1^2\sigma_{\epsilon,t}^2)\mathbf{I}\big)\,. \quad (17)$$

We see that the mean matches the original forward process, but variance includes an additional quantization-dependent term $C_1^2\sigma_{\epsilon,t}^2$. As a result, quantized marginal distribution $q'(\boldsymbol{x}_{t-1}|\boldsymbol{x}_0)$ no longer coincides with the forward marginal of any discrete timestep in the original diffusion schedule.

To restore equivalence, we introduce a scaling factor C_2 and a shifted timestep $\tau > t-1$ such that:

$$q(C_2\boldsymbol{x}_\tau|\boldsymbol{x}_0) = \mathcal{N}\big(C_2\boldsymbol{x}_\tau; C_2\sqrt{\bar{\alpha}_\tau}\boldsymbol{x}_0, C_2^2(1-\bar{\alpha}_\tau)\mathbf{I}\big)\,. \quad (18)$$

It can be shown that setting $C_2 = \sqrt{1 + C_1^2\sigma_{\epsilon,t}^2}$ and $\bar{\alpha}_\tau = \bar{\alpha}_{t-1}/C_2^2$ makes $q'(\boldsymbol{x}_{t-1}|\boldsymbol{x}_0)$ and $q(C_2\boldsymbol{x}_\tau|\boldsymbol{x}_0)$ statistically equivalent. This establishes quantization as a *timestep shift* in diffusion process.

Deformable Noise Scheduler Building on this insight, we introduce the *Deformable Noise Scheduler (DNS)*, which maps quantized diffusion states to adjusted timesteps in the full-precision schedule. From Eq. 18, the mapping Φ is:

$$\boldsymbol{x}_\tau = \Phi(\boldsymbol{x}_{t-1}) = \boldsymbol{x}_{t-1}/C_2. \quad (19)$$

Direct application, however, faces two challenges: (i) τ is typically non-integer, complicating integration into discrete samplers, and (ii) rounding τ introduces additional error and potentially extra denoising steps.

To avoid this, we redesign the scheduler by redefining the variance schedule at the previous timestep in the quantized process as $\bar{\alpha}_{t-1}^q$. From Eq. 18, we obtain:

$$\bar{\alpha}_\tau = \frac{\bar{\alpha}_{t-1}^q}{1 + C_1^2\sigma_{\epsilon,t}^2}. \quad (20)$$

Solving Eq. 20 for $\bar{\alpha}_{t-1}^q$ aligns τ with $t-1$, ensuring that quantized updates maintain consistent with the original diffusion timesteps.

DNS thus dynamically adapts the noise schedule according to $\sigma_{\epsilon,t}^2$, preserving distributional equivalence without introducing additional steps or overhead. By the same reasoning, DNS naturally extends to flow-matching with Gaussian conditional paths (see Appendix A.3).

5. Experiments

5.1. Settings

Models and Datasets We benchmark our method using LDM-4 (Rombach et al., 2022), DiT-XL (Peebles & Xie, 2023), and FLUX.1 (Labs, 2024) (Flow-matching). Following previous works (Li et al., 2025), we randomly sample 3,000 text prompts from COCO Captions 2014 (Chen et al., 2015) for calibration. This calibration set is used to determine the quantization parameters and estimate noise characteristics across all models. For our evaluation datasets, we

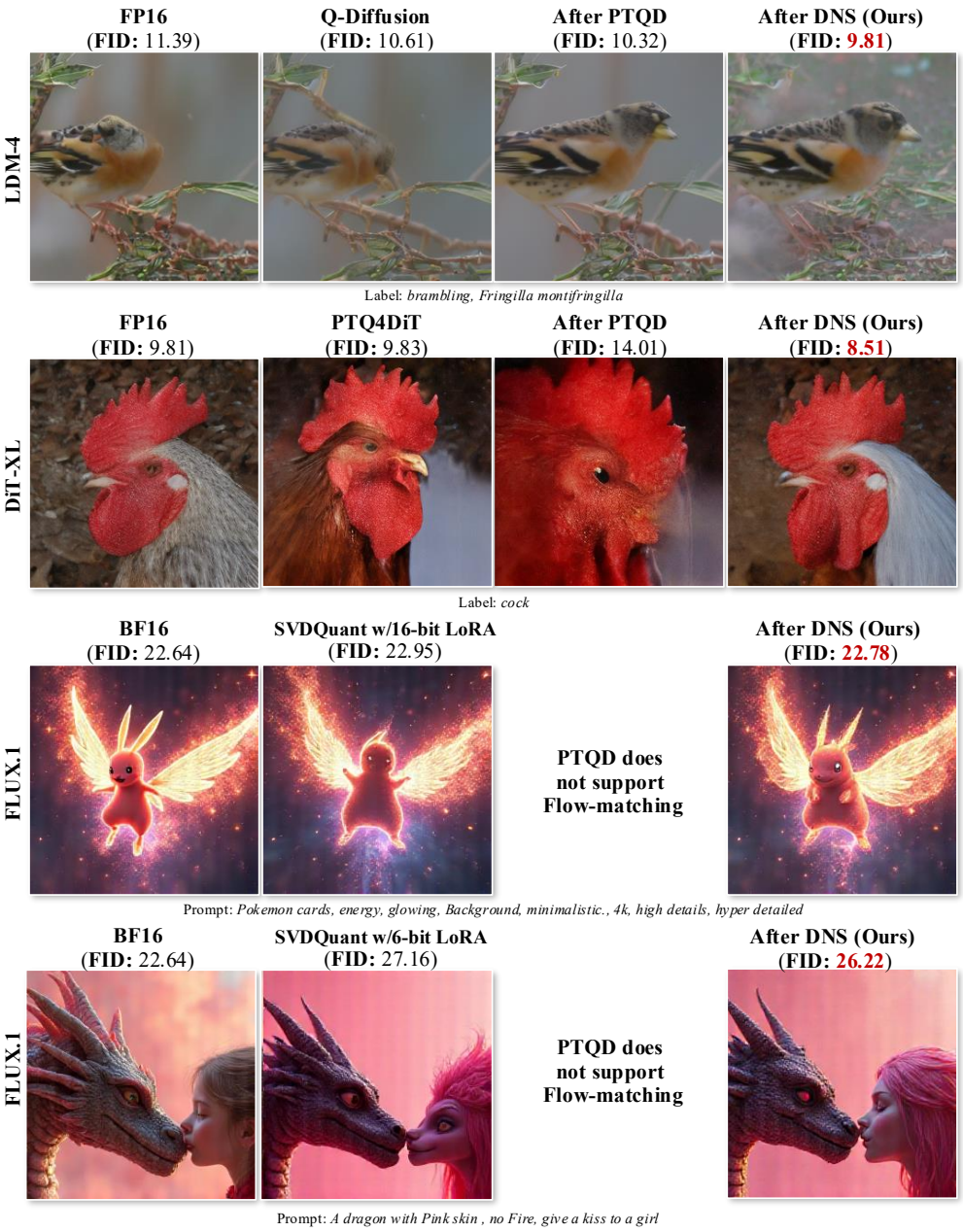

Figure 6. We tested the results on several models (including diffusion and Flow-matching) and compared the results of our method with FP, PTQ, PTQ+PTQD. Numbers in brackets are FID↓.

use ImageNet for class-conditional generation. For text-to-image generation, we use the MJHQ-30K dataset (Li et al., 2024). Our experiments were conducted on a NVIDIA A100-40G GPU. However, it should be noted that our method does not require additional memory usage, as the main storage cost is about network parameters. Both LDM and DIT-XL can run on smaller GPUs.

Baselines We compare our method with several PTQ techniques. (1) LDM-4: Tested with 20 steps, guidance scale 3.0, and 256×256 resolution. We compare the FP16 model, Q-Diffusion (W4A8) (Li et al., 2023), and its combination with PTQD (He et al., 2023). (2) DiT-XL: Evaluated with 20 steps, guidance scale 1.5, and 256×256 resolution. We compare the FP16 model, PTQ4DiT (W4A8) (Wu et al., 2024), and its combination with PTQD. (3) FLUX.1: Tested with 20 steps, guidance scale 3.5, and 256×256 resolution. The original SVDQuant relies on a W16A16 LoRA branch, which prevents a fully quantized integer inference pipeline. To eliminate the overhead of mixed-

Table 1. Performance comparison across different models

Model	Bit	Method	Evaluation Metrics					
			FID↓	sFID↓	IS↑	CLIP↑	IR↑	PSNR↑
LDM-4	FP16	-	11.49	9.99	104.74	31.91	0.134	-
	W4A8	Q-Diffusion	10.68	13.71	101.95	31.97	-0.014	22.84
		w/PTQD	10.32	12.39	100.84	31.89	-0.031	23.13
		w/ours	**9.81**	**9.42**	**102.40**	31.91	**0.015**	23.10
DiT-XL	FP16	-	9.81	21.11	76.09	29.84	-0.349	-
	W4A8	PTQ4DiT	9.83	17.52	70.79	29.92	-0.508	17.42
		w/PTQD	14.01	17.13	64.67	29.73	-0.609	16.32
		w/ours	**8.51**	**16.64**	**72.65**	**30.01**	**-0.484**	**17.43**
FLUX.1	BF16	-	22.64	54.23	24.15	29.30	0.900	-
	W4A4 *w*/W16 LoRA	SVDQuant	22.95	53.64	23.80	29.21	0.877	22.21
		w/ours	**22.78**	**53.15**	**24.01**	29.21	**0.890**	21.92
	W4A4 *w*/W6 LoRA	SVDQuant	27.16	58.15	22.68	28.89	0.693	16.17
		w/ours	**26.22**	**57.36**	**23.58**	**29.01**	**0.709**	15.87

precision computing and enable compatibility with integer-constrained edge devices, we further quantized the LoRA branch of SVDQuant to 6-bit weight. We compare the BP16 model and SVDQuant (W4A4) with W16A16 and W6A16 LoRA (Li et al., 2025). PTQD does not support flow-matching models.

Metrics Following previous works (Li et al., 2025), we evaluate generation quality using several metrics. Fréchet Inception Distance (FID (Heusel et al., 2017; Parmar et al., 2022)) and sliding Fréchet Inception Distance (sFID (Ding et al., 2022)) are particularly well-suited for reflecting distribution similarity, as it measures the distance between feature distributions extracted from generated and real data using a pre-trained neural network. Inception Score (IS (Salimans et al., 2016)) aims to assess quality and diversity. CLIPScore (CLIP (Hessel et al., 2021)) aims to measure text-image alignment. Image Reward (IR (Xu et al., 2023)) aims to approximate human judgment. We also employ Peak Signal Noise Ratio (PSNR) to measures pixel-level trajectory difference, but this metric cannot validate whether the final outputs achieve better distribution preservation or generation quality. Note that in class-conditional generation we use the tag name with scientific nomenclature to calculate IR.

5.2. Main Results

We present our main results in Tab.1 and Fig.6. For class-conditional experiments we generate 30,000 images, and for text-to-image (MJHQ) we generate 10,000 images for evaluation. Observing our experimental results, we find substantial improvements in generation quality metrics including FID (8.1%-13.4% improvement), IS, and IR, demonstrating that our method effectively preserves the original data distribution. Although PSNR decreases slightly in some settings (0.1%-1.6%), CLIP scores remain essentially unchanged ($\leqslant 0.2\%$), confirming that semantic alignment with text conditions is preserved. Since CLIP scores confirm semantic consistency, the PSNR differences reflect different high-quality sampling paths under identical semantic constraints, not semantic drift(worse CLIP) or quality loss(worse FID).

Specifically, for LDM-4 quantized to W4A8 with Q-Diffusion, our approach outperforms both the baseline quantized model and PTQD, improving FID from 10.68 to 9.81 and IR from -0.014 to 0.015. For DiT-XL with PTQ4DiT at W4A8, PTQD exhibits marked instability at W4A8 and fails to produce acceptable results; in contrast, our method is robust, improving FID from 9.83 to 8.51 (W4A8). For FLUX.1 under flow matching with SVDQuant at W4A4 with full precision LoRA, even where the baseline quantization method performs exceptionally close to full precision, our method applies directly and further improves results, reducing FID from 22.95 to 22.78 and increasing IR from 0.877 to 0.890. For the configuration with 6-bit LoRA, all weights required for network inference are constrained to 6 bits or less. This implies that the entire model can be executed using efficient integer arithmetic without switching to floating-point operations. Although the LoRA branch quantized model increases FID from 22.64 to 27.16. After applying our DNS method decrease FID from 27.16 to 26.22. More visualizations are provided in Appendix A.4.

5.3. Ablation

More ablation experiments are provided in Appendix A.5.

6. Conclusion

In this paper, we have introduced a novel quantization error absorbing method for diffusion models that effectively mitigates quality degradation after quantization. Unlike previous method, our method is distribution-preserving: it explicitly aligns the quantized model's process distribution with the unquantized diffusion distribution. And our solution works across stochastic, deterministic, and Flow-matching frameworks with Gaussian conditional probability paths. Extensive experiments validate that our method significantly improves generation quality in quantized diffusion models while maintaining computational efficiency.

Acknowledgements

This research was conducted by ACCESS – AI Chip Center for Emerging Smart Systems, supported by the InnoHK initiative of the Innovation and Technology Commission of the Hong Kong Special Administrative Region Government.

The work has been supported by Hong Kong Research Grant Council - General Research Fund Scheme (Grant No. 17202422, 17212923, 17215025) Theme-based Research (Grant No.T45-701/22-R), and Strategic Topics Grant (Grant No.STG3/E-605/25-N). Part of the described research work is conducted in the JC STEM Lab of Robotics for Soft Materials funded by The Hong Kong Jockey Club Charities Trust.

Impact Statement

This paper presents work whose goal is to advance the field of Machine Learning. There are many potential societal consequences of our work, none which we feel must be specifically highlighted here.

References

Bińkowski, M., Sutherland, D. J., Arbel, M., and Gretton, A. Demystifying mmd gans, 2021. URL https://arxiv.org/abs/1801.01401.

Brooks, T., Peebles, B., Holmes, C., DePue, W., Guo, Y., Jing, L., Schnurr, D., Taylor, J., Luhman, T., Luhman, E., Ng, C., Wang, R., and Ramesh, A. Video generation models as world simulators. 2024. URL https://openai.com/research/video-generation-models-as-world-simulators.

Chen, J., Yu, J., Ge, C., Yao, L., Xie, E., Wu, Y., Wang, Z., Kwok, J., Luo, P., Lu, H., and Li, Z. Pixart-α: Fast training of diffusion transformer for photorealistic text-to-image synthesis, 2023. URL https://arxiv.org/abs/2310.00426.

Chen, X., Fang, H., Lin, T.-Y., Vedantam, R., Gupta, S., Dollár, P., and Zitnick, C. L. Microsoft coco captions: Data collection and evaluation server. *arXiv preprint arXiv:1504.00325*, 2015.

Chi, C., Xu, Z., Feng, S., Cousineau, E., Du, Y., Burchfiel, B., Tedrake, R., and Song, S. Diffusion policy: Visuomotor policy learning via action diffusion. *The International Journal of Robotics Research*, 2024.

Ding, X., Wang, Y., Xu, Z., Welch, W. J., and Wang, Z. J. Continuous conditional generative adversarial networks: Novel empirical losses and label input mechanisms. *IEEE Transactions on Pattern Analysis and Machine Intelligence*, 45(7):8143–8158, 2022.

He, Y., Liu, L., Liu, J., Wu, W., Zhou, H., and Zhuang, B. Ptqd: Accurate post-training quantization for diffusion models. *arXiv preprint arXiv:2305.10657*, 2023.

Hessel, J., Holtzman, A., Forbes, M., Bras, R. L., and Choi, Y. CLIPscore: A reference-free evaluation metric for image captioning. *arXiv preprint arXiv:2104.08718*, 2021.

Heusel, M., Ramsauer, H., Unterthiner, T., Nessler, B., and Hochreiter, S. GANs trained by a two time-scale update rule converge to a local Nash equilibrium. *Advances in neural information processing systems*, 30, 2017.

Ho, J., Jain, A., and Abbeel, P. Denoising diffusion probabilistic models, 2020. URL https://arxiv.org/abs/2006.11239.

Huang, Y., Gong, R., Liu, J., Chen, T., and Liu, X. Tfmq-dm: Temporal feature maintenance quantization for diffusion models, 2024. URL https://arxiv.org/abs/2311.16503.

Jacob, B., Kligys, S., Chen, B., Zhu, M., Tang, M., Howard, A., Adam, H., and Kalenichenko, D. Quantization and training of neural networks for efficient integer-arithmetic-only inference, 2017. URL https://arxiv.org/abs/1712.05877.

Labs, B. F. Flux. https://github.com/black-forest-labs/flux, 2024.

Li, D., Kamko, A., Akhgari, E., Sabet, A., Xu, L., and Doshi, S. Playground v2.5: Three insights towards enhancing aesthetic quality in text-to-image generation, 2024. URL https://arxiv.org/abs/2402.17245.

Li, M., Lin, Y., Zhang, Z., Cai, T., Li, X., Guo, J., Xie, E., Meng, C., Zhu, J.-Y., and Han, S. Svdquant: Absorbing outliers by low-rank components for 4-bit diffusion models, 2025. URL https://arxiv.org/abs/2411.05007.

Li, X., Liu, Y., Lian, L., Yang, H., Dong, Z., Kang, D., Zhang, S., and Keutzer, K. Q-diffusion: Quantizing diffusion models, 2023. URL https://arxiv.org/abs/2302.04304.

Lipman, Y., Chen, R. T. Q., Ben-Hamu, H., Nickel, M., and Le, M. Flow matching for generative modeling, 2023. URL https://arxiv.org/abs/2210.02747.

Nagel, M., Fournarakis, M., Amjad, R. A., Bondarenko, Y., van Baalen, M., and Blankevoort, T. A white paper on neural network quantization, 2021. URL https://arxiv.org/abs/2106.08295.

Parmar, G., Zhang, R., and Zhu, J.-Y. On aliased resizing and surprising subtleties in GAN evaluation. In *Proceedings of the IEEE/CVF conference on computer vision and pattern recognition*, pp. 11410–11420, 2022.

Peebles, W. and Xie, S. Scalable diffusion models with transformers, 2023. URL https://arxiv.org/abs/2212.09748.

Podell, D., English, Z., Lacey, K., Blattmann, A., Dockhorn, T., Müller, J., Penna, J., and Rombach, R. Sdxl: Improving latent diffusion models for high-resolution image synthesis, 2023. URL https://arxiv.org/abs/2307.01952.

Qi, T., Fang, S., Wu, Y., Xie, H., Liu, J., Chen, L., He, Q., and Zhang, Y. Deadiff: An efficient stylization diffusion model with disentangled representations, 2024. URL https://arxiv.org/abs/2403.06951.

Rombach, R., Blattmann, A., Lorenz, D., Esser, P., and Ommer, B. High-resolution image synthesis with latent diffusion models, 2022. URL https://arxiv.org/abs/2112.10752.

Salimans, T., Goodfellow, I., Zaremba, W., Cheung, V., Radford, A., and Chen, X. Improved techniques for training GANs. *Advances in neural information processing systems*, 29, 2016.

Shang, Y., Yuan, Z., Xie, B., Wu, B., and Yan, Y. Post-training quantization on diffusion models, 2023. URL https://arxiv.org/abs/2211.15736.

Sohl-Dickstein, J., Weiss, E. A., Maheswaranathan, N., and Ganguli, S. Deep unsupervised learning using nonequilibrium thermodynamics, 2015. URL https://arxiv.org/abs/1503.03585.

Song, J., Meng, C., and Ermon, S. Denoising diffusion implicit models, 2022. URL https://arxiv.org/abs/2010.02502.

Wang, C., Wang, Z., Xu, X., Tang, Y., Zhou, J., and Lu, J. Towards accurate post-training quantization for diffusion models, 2024. URL https://arxiv.org/abs/2305.18723.

Wu, J., Wang, H., Shang, Y., Shah, M., and Yan, Y. Ptq4dit: Post-training quantization for diffusion transformers, 2024. URL https://arxiv.org/abs/2405.16005.

Xu, J., Liu, X., Wu, Y., Tong, Y., Li, Q., Ding, M., Tang, J., and Dong, Y. Imagereward: Learning and evaluating human preferences for text-to-image generation. *Advances in Neural Information Processing Systems*, 36: 15903–15935, 2023.

Ye, J., Wang, Z., and Jiang, L. Pqd: Post-training quantization for efficient diffusion models, 2024. URL https://arxiv.org/abs/2501.00124.

Zhang, R., Isola, P., Efros, A. A., Shechtman, E., and Wang, O. The unreasonable effectiveness of deep features as a perceptual metric, 2018. URL https://arxiv.org/abs/1801.03924.

Zhao, T., Ning, X., Fang, T., Liu, E., Huang, G., Lin, Z., Yan, S., Dai, G., and Wang, Y. Mixdq: Memory-efficient few-step text-to-image diffusion models with metric-decoupled mixed precision quantization, 2024. URL https://arxiv.org/abs/2405.17873.

Zheng, X., Liu, X., Bian, Y., Ma, X., Zhang, Y., Wang, J., Guo, J., and Qin, H. Bidm: Pushing the limit of quantization for diffusion models, 2024. URL https://arxiv.org/abs/2412.05926.

Zhou, J., Zhang, W., and Liu, Y.-S. Diffgs: Functional gaussian splatting diffusion, 2024. URL https://arxiv.org/abs/2410.19657.

A. Appendix

A.1. Details of Kurtosis-Based Uniform Noise Compensation

Kurtosis measures the "tailedness" of a probability distribution, indicating whether data has heavy tails (more outliers) or light tails compared to a normal distribution. For a random variable x with mean μ, its kurtosis is defined as:

$$\kappa_x = \frac{\mathbb{E}[(X-\mu)^4]}{(\mathbb{E}[(X-\mu)^2])^2} - 3 \tag{21}$$

A positive kurtosis suggests heavier tails and a sharper peak, while a negative kurtosis indicates lighter tails and a flatter distribution. For instance, a Gaussian variable has a kurtosis of 0 while that of a uniform variable is -1.2.

To compensate for the positive kurtosis κ_o of residual noise with variance σ_o^2, we introduce uniform noise with variance σ_u^2 and kurtosis $\kappa_u < 0$. Given that the two are independent, the kurtosis of their summation can be easily obtained:

$$\kappa_{new} = \frac{\kappa_o \cdot \sigma_o^4 + \kappa_u \cdot \sigma_u^4}{(\sigma_o^2 + \sigma_u^2)^2} \tag{22}$$

Setting κ_{new} to zero and substituting $\kappa_u = -1.2$, we have:

$$\sigma_u^2 = \sigma_o^2 \cdot \sqrt{\frac{5\kappa_o}{6}} \tag{23}$$

Consequently, the compensated noise has a variance of $\sigma_{new}^2 = \sigma_o^2 \cdot \left(1 + \sqrt{\frac{5\kappa_o}{6}}\right)$ and a kurtosis of 0, which can be regarded as a Gaussian distribution.

The uniform distribution is an attractive choice for DCNC because it's kurtosis is very low(excess kurtosis -1.2) and can be sampled efficiently on standard hardware. Unless otherwise stated, all experiments in paper use uniform distribution as the compensation distribution in DCNC.

More Statistical Analysis In order to more clearly demonstrate that the compensated residual distribution is closer to a Gaussian, we further measure skewness and higher-order central moments of the residuals. excess kurtosis. Based on the definition of kurtosis, we also define a sixth-order excess kurtosis $\kappa_6 = \frac{\mu_6}{\sigma^6} - 15$ which equals 0 for a Gaussian distribution. We collect the outputs of the LDM-4 model with Q-Diffusion quantized to W4A8 and compute the above statistics over residuals. Results for part of representative timesteps are shown in Tab. 2.

We further visualize the comparison of Kurtosis and Sixth-order Kurtosis before and after DCNC in Fig. 4 and Fig. 7. We also summarize statistics over all timesteps with error bars in Tab. 3.

Table 2. Statistical moments of quantization noise before and after DCNC

Timestep	Skewness	κ_x	κ_x w/DCNC	μ_5	κ_6	κ_6 w/DCNC
950	0.26×10^{-2}	-0.07	-0.07	1.03×10^{-8}	-0.47	-0.47
850	0.24×10^{-2}	-0.01	-0.10	0.03×10^{-8}	-0.85	-0.85
750	0.07×10^{-2}	-0.09	-0.09	0.39×10^{-8}	-0.40	-0.40
650	-0.51×10^{-2}	0.21	-0.02	-9.29×10^{-8}	9.18	0.81
550	-0.94×10^{-2}	3.30	0.08	-0.03×10^{-4}	81.38	6.28
450	-0.88×10^{-2}	3.34	0.14	-0.16×10^{-4}	145.49	9.45
350	-0.62×10^{-2}	2.33	0.15	-0.28×10^{-4}	138.41	9.75
250	-0.39×10^{-2}	1.78	0.14	-0.52×10^{-4}	101.13	8.82
150	-0.36×10^{-2}	1.33	0.10	-1.59×10^{-4}	68.45	7.23
50	-0.51×10^{-2}	1.11	0.08	-9.26×10^{-4}	48.54	5.82

In these tables, the skewness and fifth-order central moment are collected after compensation, and sixth-order excess kurtosis κ_6 is collected both before and after compensation for comparison. The results show that, after compensation, skewness and the fifth moment(odd-order moments) are close to zero, indicating that the residuals are nearly symmetric. At the same time, both excess kurtosis and sixth-order excess kurtosis κ_6 are substantially reduced, providing additional evidence that DCNC makes the residual distribution significantly closer to a Gaussian.

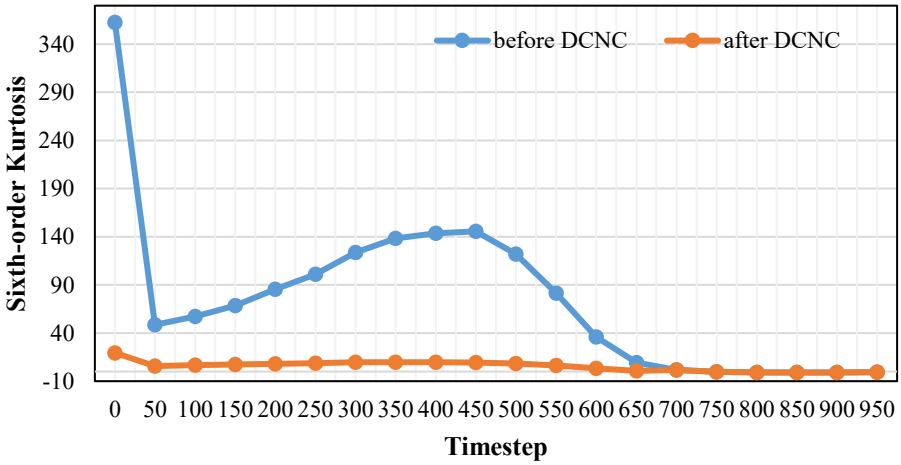

Figure 7. Sixth-order Kurtosis before and after DCNC.

Table 3. Statistics over all timesteps with error bars.

Skewness ($\times 10^{-3}$)	κ_x	κ_x w/DCNC	μ_5 ($\times 10^{-4}$)	κ_6	κ_6 w/DCNC
-3.65 ± 4.15	1.42 ± 1.38	0.02 ± 0.12	-1.30 ± 2.85	76.09 ± 86.71	5.57 ± 5.25

More Low-kurtosis Distribution Choices Besides uniform distribution, there exist many other low-kurtosis choices that can be used for compensation. In this work we consider four such noise distribution : uniform distribution $U(-a, a)$ (κ=-1.2), symmetric triangular distribution on $[-a, a]$ (κ=-0.6), bimodal Gaussian mixture (κ=-0.5 with r=1), and generalized Gaussian (exponential-power) distribution(thus $\kappa \approx$-0.81 with β=4). Ablation results over these distributions are shown in Tab. 4.

Table 4. Effect of different compensation distributions in DCNC

DCNC distribution	FID↓	sFID↓	IS↑
Uniform	9.65	9.33	101.96
Triangular	9.60	9.14	102.30
Bimodal Gaussian mixture	9.77	9.69	101.60
Generalized Gaussian	9.66	9.35	102.04

From this table, we observe that the triangular distribution achieves better overall performance than uniform distribution, indicating that using a triangular noise distribution for DCNC compensation is also a viable choice. Nevertheless, due to uniform distribution extremely simple and efficient sampling properties on standard hardware, we retain the uniform distribution as the default compensation distribution throughout this paper.

A.2. Extended Details and Supplementary Material for the Main Derivation

In Sec. 4.1, I derived the transformation function T. Next, I will provide a detailed derivation of the transformation function T.

From Eq. 8 and Eq. 11, we have:

$$\frac{\epsilon'_\theta(\boldsymbol{x}_t, t)}{1+k} = \epsilon_\theta(\boldsymbol{x}_t, t) + \frac{\Delta'\epsilon_\theta(\boldsymbol{x}_t, t)}{1+k} \tag{24}$$

Following the idea of PTQD, we can treat the latter term as random noise, $\frac{\Delta'\epsilon_\theta(\boldsymbol{x}_t,t)}{1+k} \approx \eta_\theta$. Experiments show that η_θ has higher kurtosis than Gaussian noise. Therefore, we introduce a uniform distribution component. Combined with compensation using Eq. 13:

$$\frac{\Delta'\epsilon_\theta(\boldsymbol{x}_t, t)}{1+k} + U(0, \sigma_u^2) = \Delta''\epsilon_\theta(0, \sigma_{\epsilon,t}) \sim \mathcal{N}(0, \sigma_{\epsilon,t}^2) \tag{25}$$

In practice, we introduce a factor W_u to control the final proportion added. The analysis of W_u is presented in Sec. 5.3. Thus, we can formulate our improved transformation T as Eq. 14:

$$T(\epsilon'_\theta(\boldsymbol{x}_t, t)) = \frac{\epsilon'_\theta(\boldsymbol{x}_t, t)}{1+k} + W_u \cdot U(0, \sigma_u^2) \tag{26}$$

$$= \epsilon_\theta(\boldsymbol{x}_t, t) + \frac{\Delta'\epsilon_\theta(\boldsymbol{x}_t, t)}{1+k} + W_u \cdot U(0, \sigma_u) \tag{27}$$

$$= \epsilon_\theta(\boldsymbol{x}_t, t) + \Delta''_{\epsilon_\theta}(0, \sigma_{\epsilon,t}) \tag{28}$$

where $\sigma_{\epsilon,t}$ and k are statistically computed from the calibration.

When employing a quantized model, quantization introduces parameter perturbations that manifest as errors in noise prediction. The noise predicted by quantized model can be represented as Eq. 11:

$$\epsilon'_\theta(\boldsymbol{x}_t, t) = \epsilon_\theta(\boldsymbol{x}_t, t) + \Delta_{\epsilon_\theta}(\boldsymbol{x}_t, t)$$

where $\epsilon_\theta(\boldsymbol{x}_t, t)$ represents the original network prediction, $\epsilon'_\theta(\boldsymbol{x}_t, t)$ represents the quantized network prediction, and $\Delta_{\epsilon_\theta}(\boldsymbol{x}_t, t)$ captures the quantization-induced error.

To ensure that the noise distribution introduced by quantization errors approximates a Gaussian distribution, we apply a transformation T to this error function Eq. 12:

$$T(\epsilon'_\theta(\boldsymbol{x}_t, t)) = \epsilon_\theta(\boldsymbol{x}_t, t) + \Delta''_{\epsilon_\theta}(0, \sigma_{\epsilon,t})$$

where $\Delta''_{\epsilon_\theta}(0, \sigma_{\epsilon,t})$ follows a Gaussian distribution with mean 0 and variance $\sigma_{\epsilon,t}^2$ that depends on the timestep t.

Substituting Eq. 12 into Eq. 3, we obtain:

$$\hat{\boldsymbol{x}}'_0 = \frac{1}{\sqrt{\bar{\alpha}_t}}(\boldsymbol{x}_t - \sqrt{1-\bar{\alpha}_t}T(\epsilon'_\theta(\boldsymbol{x}_t, t))) \tag{29}$$

$$= \frac{1}{\sqrt{\bar{\alpha}_t}}(\boldsymbol{x}_t - \sqrt{1-\bar{\alpha}_t}\epsilon_\theta(\boldsymbol{x}_t, t)) - \frac{\sqrt{1-\bar{\alpha}_t}}{\sqrt{\bar{\alpha}_t}}\Delta''_{\epsilon_\theta}(0, \sigma_{\epsilon,t}) \tag{30}$$

$$= \hat{\boldsymbol{x}}_0 - \frac{\sqrt{1-\bar{\alpha}_t}}{\sqrt{\bar{\alpha}_t}}\Delta''_{\epsilon_\theta}(0, \sigma_{\epsilon,t}) \tag{31}$$

where the estimation of $\boldsymbol{x}_0$ using the quantized model, denoted as $\hat{\boldsymbol{x}}'_0$. Consequently, the reverse process under quantization

is shown as Eq. 15:

$$p'_\theta(\boldsymbol{x}_{t-1} \mid \boldsymbol{x}_t) = \mathcal{N}\left(\sqrt{\bar{\alpha}_{t-1}}\boldsymbol{x}'_0 + \sqrt{1-\bar{\alpha}_{t-1}-\sigma_t^2} \cdot \frac{\boldsymbol{x}_t - \sqrt{\bar{\alpha}_t}\boldsymbol{x}'_0}{\sqrt{1-\bar{\alpha}_t}}, \sigma_t^2 I_1\right) \tag{32}$$

$$= \mathcal{N}\left(\sqrt{\bar{\alpha}_{t-1}}\boldsymbol{x}_0 + \sqrt{1-\bar{\alpha}_{t-1}-\sigma_t^2} \cdot \frac{\boldsymbol{x}_t - \sqrt{\bar{\alpha}_t}\boldsymbol{x}_0}{\sqrt{1-\bar{\alpha}_t}} + C_1\Delta''_{\epsilon_\theta}(0, \sigma_{\epsilon,t}), \sigma_t^2 I\right) \tag{33}$$

$$= \mathcal{N}\left(\sqrt{\bar{\alpha}_{t-1}}\boldsymbol{x}_0 + \sqrt{1-\bar{\alpha}_{t-1}-\sigma_t^2} \cdot \frac{\boldsymbol{x}_t - \sqrt{\bar{\alpha}_t}\boldsymbol{x}_0}{\sqrt{1-\bar{\alpha}_t}}, \sigma_t^2 I_+ C_1^2\sigma_{\epsilon,t}^2 I\right) \tag{34}$$

When using the DDIM sampler for deterministic sampling, $\sigma_t = 0$.

Then we derive the marginal distribution $q'(\boldsymbol{x}_{t-1}|\boldsymbol{x}_0)$ by integrating over the intermediate variable $\boldsymbol{x}_t$:

$$q'(\boldsymbol{x}_{t-1}|\boldsymbol{x}_0) = \int q_\sigma(\boldsymbol{x}_{t-1}|\boldsymbol{x}_t, \boldsymbol{x}_0) \cdot q(\boldsymbol{x}_t|\boldsymbol{x}_0)\, d\boldsymbol{x}_t \tag{35}$$

Rigorously deriving this integral is quite complex, so we first provide a simplified derivation. We need to know that any linear combination and marginalization of Gaussian distributions remains Gaussian, allowing us to consider the mean and variance of the integral result separately.

Observing Eq. 34, we find that quantization only affects the variance part of $q'(\boldsymbol{x}_{t-1}|\boldsymbol{x}_t, \boldsymbol{x}_0)$, while the mean part remains unchanged.

First is mean analysis: Since the added variance terms have zero mean, by the law of total expectation, the marginal mean remains unchanged:

$$E[q'(\boldsymbol{x}_{t-1}|\boldsymbol{x}_0)] = E[E[q'(\boldsymbol{x}_{t-1}|\boldsymbol{x}_t, \boldsymbol{x}_0)]|\boldsymbol{x}_0] = \sqrt{\bar{\alpha}_{t-1}}\boldsymbol{x}_0 \tag{36}$$

Then is Variance Analysis: We apply the law of total variance:

$$\text{Var}[q'(\boldsymbol{x}_{t-1}|\boldsymbol{x}_0)] = E[\text{Var}[q'(\boldsymbol{x}_{t-1}|\boldsymbol{x}_t, \boldsymbol{x}_0)]|\boldsymbol{x}_0] + \text{Var}[q'(E[\boldsymbol{x}_{t-1}|\boldsymbol{x}_t, \boldsymbol{x}_0)]|\boldsymbol{x}_0] \tag{37}$$

since the first term's independent of $\boldsymbol{x}_t$:

$$E[\sigma_t^2 I_1 + C_t^2\sigma_\epsilon^2 I_2|\boldsymbol{x}_0] = (\sigma_t^2 + C_t^2\sigma_\epsilon^2)\mathbf{I} \tag{38}$$

Since the added variance terms have zero mean, the second term remains consistent with the original diffusion process:

$$\text{Var}[E[q'(\boldsymbol{x}_{t-1}|\boldsymbol{x}_t, \boldsymbol{x}_0)]|\boldsymbol{x}_0] = (1-\bar{\alpha}_{t-1}-\sigma_t^2)\mathbf{I} \tag{39}$$

Therefore, the final integral result is Eq. 17:

$$q'(\boldsymbol{x}_{t-1}|\boldsymbol{x}_0) = \mathcal{N}(\boldsymbol{x}_{t-1}; \sqrt{\bar{\alpha}_{t-1}}\boldsymbol{x}_0, (1-\bar{\alpha}_{t-1}+C_1^2\sigma_{\epsilon,t}^2)\mathbf{I})$$

Consequently, the quantized model marginal distribution $q'(\boldsymbol{x}_{t-1}|\boldsymbol{x}_0)$ does not directly map the data distribution of the original generative process.

To address this, we seek a transformation that maps it to the original diffusion marginal distribution at other timesteps. We introduce a scaling factor C_2 and a new timestep τ that together establish an equivalence between the marginal distribution of the quantized model and that of the original diffusion model. Specifically, we define Eq. 18:

$$q(C_2\boldsymbol{x}_\tau|\boldsymbol{x}_0) = \mathcal{N}(C_2\boldsymbol{x}_\tau; C_2\sqrt{\bar{\alpha}_\tau}\boldsymbol{x}_0, C_2^2(1-\bar{\alpha}_\tau)\mathbf{I})$$

Through multi-step denoising, this marginal distribution mapping ensures that the final generated distribution matches the original model's distribution. To make $q(\boldsymbol{x}'_{t-1}|\boldsymbol{x}_0)$ and $q(C_2\boldsymbol{x}_\tau|\boldsymbol{x}_0)$ in Eq. 17 and Eq. 18 statistically equivalent, we set their means and variances equal respectively.

Therefore, we solve the system of equations:

$$\begin{cases} \sqrt{\bar{\alpha}_{t-1}} = C_2\sqrt{\bar{\alpha}_\tau} & \text{(mean equality)} \\ (1-\bar{\alpha}_{t-1}) + C_1^2\sigma_{\epsilon,t}^2 = C_2^2(1-\bar{\alpha}_\tau) & \text{(variance equality)} \end{cases} \tag{40}$$

Algorithm 1 Deformable Noise Scheduler Calibration

Input: Timesteps sequence $\{(t, t_{\text{prev}})\}$, Calibration set $C = \{\boldsymbol{x}_0\}$
Output: Calibrated alpha values $\{\bar{\alpha}^q_{t-1}(t)\}$, slopes $\{k(t)\}$, uniform variances $\{\sigma^2_{\text{u}}(t)\}$
Initialize $C_\epsilon \leftarrow \emptyset$, $C_{\Delta\epsilon} \leftarrow \emptyset$
for each $(t, \text{previous } t) \in$ timesteps **do**
  for each $\boldsymbol{x}_0 \in C$ **do**
    $\boldsymbol{x}_t \leftarrow \text{AddNoise}(\boldsymbol{x}_0, t)$
    $\epsilon_\theta(\boldsymbol{x}_t) \leftarrow \text{OriginalNetwork}(\boldsymbol{x}_t)$
    $\epsilon'_\theta(\boldsymbol{x}_t) \leftarrow \text{QuantizedNetwork}(\boldsymbol{x}_t)$
    $\Delta\epsilon_\theta \leftarrow \epsilon'_\theta(\boldsymbol{x}_t) - \epsilon_\theta(\boldsymbol{x}_t)$
    $C_\epsilon.\text{append}(\epsilon_\theta(\boldsymbol{x}_t))$, $C_{\Delta\epsilon}.\text{append}(\Delta\epsilon_\theta)$
  end for
  $k(t), d(t) \leftarrow \text{LinearRegression}(C_\epsilon, C_{\Delta\epsilon})$
  $C_{\Delta'\epsilon} \leftarrow \text{ComputeResiduals}(C_\epsilon, C_{\Delta\epsilon}, k(t), d(t))$
  $\sigma^2_{\epsilon,t,\text{o}} \leftarrow \text{Variance}(C_{\Delta'\epsilon})$
  $\kappa_\text{o} \leftarrow \text{Kurtosis}(C_{\Delta'\epsilon})$
  $\sigma^2_{\text{u}}(t) \leftarrow \sigma^2_{\epsilon,t,\text{o}} \times \sqrt{\frac{5\kappa_\text{o}}{6}}$ *// from Eq.(14)*
  $C_{\Delta''\epsilon} \leftarrow \text{Transformation}T(C_{\Delta'\epsilon}, k(t), W_\text{u}, \sigma^2_\text{u}(t))$ *// from Eq.(15)*
  $\sigma^2_{\epsilon,t} \leftarrow \text{Variance}(C_{\Delta''\epsilon})$
  $\bar{\alpha}^q_{t-1} \leftarrow \text{NewtonSolve}\left(\bar{\alpha}_{t-1} = \frac{\bar{\alpha}^q_{t-1}}{1+C_1^2\sigma^2_{\epsilon,t}}\right)$ *// from Eq.(13)*
  Store $\bar{\alpha}^q_{t-1}(t)$, $k(t)$, $\sigma^2_\text{u}(t)$
end for
Return $\{\bar{\alpha}^q_{t-1}(t)\}$, $\{k(t)\}$, $\{\sigma^2_\text{u}(t)\}$

Note: Linear regression models $\Delta\epsilon_\theta = k(t) \cdot \epsilon_\theta + d(t) + \text{residual}$, but $d(t)$ is usually very close to 0.

Solving this system yields:

$$C_2 = \sqrt{1 + C_1^2\sigma^2_{\epsilon,t}} \quad \text{and} \quad \bar{\alpha}_\tau = \frac{\bar{\alpha}_{t-1}}{C_2^2} \tag{41}$$

While PTQD (He et al., 2023) also attempt to absorb quantization error into noise terms, our method provides a principled mathematical framework that explicitly maps the quantized distribution back to the forward diffusion process by timestep shift. The resulting compensation mechanism is theoretically guaranteed to perform effectively across stochastic sampling, deterministic sampling, and Flow-matching with Gaussian conditional probability paths. Through absorbing quantization error by timestep shift, our approach provides a more fundamental understanding of quantization in diffusion models while offering practical advantages in implementation flexibility and sampling robustness.

Based on the above derivations, the implementation is given in Algorithm 1 and Algorithm 2.

A side-by-side derivation comparing our DNS to PTQD is shown in Tab. 5.

We also draw a concise comparison table to better compare our method with prior work, shown in Tab. 6

This highlights that DNS is both plug-and-play over many existing PTQ methods and applicable to stochastic(Stoch.), deterministic(Det.), and flow-matching(FM) samplers without architectural/weight changes or additional training.

Algorithm 2 Deformable Noise Scheduler Inference

Input: Calibrated parameters $\{\bar{\alpha}^q_{t-1}(t)\}$, $\{k(t)\}$, $\{\sigma^2_{\mathrm{u}}(t)\}$, Timesteps sequence $\{(t, \text{previous } t)\}$
Output: Generated sample $\boldsymbol{x}_0$
Initialize $\boldsymbol{x}_T \sim \mathcal{N}(0, I)$
$\boldsymbol{x}_t \leftarrow \boldsymbol{x}_T$
for each $(t, _) \in$ timesteps **do**
  $\epsilon'_\theta(\boldsymbol{x}_t, t) \leftarrow \text{QuantizedNetwork}(\boldsymbol{x}_{\text{current}}, t)$
  $\epsilon_\theta \leftarrow \text{Transformation}T(\epsilon'_\theta(\boldsymbol{x}_t, t), k(t), W_{\mathrm{u}}, \sigma^2_{\mathrm{u}}(t))$ *// from Eq.(15)*
  $\hat{\boldsymbol{x}}_0 \leftarrow \frac{\boldsymbol{x}_t - \sqrt{1-\bar{\alpha}_t}\epsilon_\theta}{\sqrt{\bar{\alpha}_t}}$ *// from Eq.(3)*
  $\boldsymbol{x}_{t-1} \leftarrow \text{DiffusionStep}(\boldsymbol{x}_t, \hat{\boldsymbol{x}}_0, t, \alpha_{t-1} = \bar{\alpha}^q_{t-1}(t), \sigma_t = 0)$ *// from Eq.(2)*
  $\boldsymbol{x}_t \leftarrow \boldsymbol{x}_{t-1}$
end for
Return $\boldsymbol{x}_t$

Note: Next loop uses t_{prev} (not t^q_{prev}) as the current timestep.

Table 5. A side-by-side derivation comparing PTQD and our DNS.

PTQD (stochastic-sampling view)	**DNS (ours, distribution-preserving view)**
Both PTQD and our DNS first decompose the quantization error (Eq. 8) as $$\Delta\epsilon_\theta(x_t, t) = k\,\epsilon_\theta(x_t, t) + \Delta'\epsilon_\theta(x_t, t).$$ This yields the following quantized conditional: $$p'_\theta(x_{t-1} \mid x_t) = \mathcal{N}\big(x_{t-1}; \hat{\mu}_t(x_t, \hat{x}_0),\, \sigma_t^2 I\big) + \xi_t,$$ $$\xi_t \sim \mathcal{N}\big(0,\, C_1^2\sigma^2_{\epsilon,t} I\big),$$ where ξ_t is the independent Gaussian component of the quantization noise. Using this decomposition and quantized conditional, PTQD then starts from the standard stochastic sampler (Eq. 5): $$x_{t-1} = \frac{1}{\sqrt{\alpha_t}}\, x_t - \beta_t \frac{1}{\sqrt{1-\bar{\alpha}_t}}\, \epsilon_\theta(x_t, t) - \sigma_t^0 z,$$ $$z \sim \mathcal{N}(0, I).$$ Substituting the decomposed quantization error into Eq. 5 gives PTQD's stochastic update (Eq. 10): $$x_{t-1} = \frac{1}{\sqrt{\alpha_t}}\, x_t - \beta_t \frac{1}{\sqrt{1-\bar{\alpha}_t}}\, \epsilon_\theta(x_t, t) - \sigma_t z - \beta_t\, c_t\, \Delta'\epsilon_\theta(x_t, t),$$ where c_t is a scalar (a function of $\alpha_t, \bar{\alpha}_t, k$), and the last two terms $-\sigma_t z - \beta_t c_t \Delta'\epsilon_\theta(x_t, t)$ jointly play the role of the original stochastic noise term $\sigma_t^0 z$ in Eq. 5. Thus $\Delta'\epsilon_\theta$ is treated as an extra stochastic noise term injected into the sampling process.	Both PTQD and our DNS first decompose the quantization error (Eq. 8) as $$\Delta\epsilon_\theta(x_t, t) = k\,\epsilon_\theta(x_t, t) + \Delta'\epsilon_\theta(x_t, t).$$ This yields the following quantized conditional: $$p'_\theta(x_{t-1} \mid x_t) = \mathcal{N}\big(x_{t-1}; \hat{\mu}_t(x_t, \hat{x}_0),\, \sigma_t^2 I\big) + \xi_t,$$ $$\xi_t \sim \mathcal{N}\big(0,\, C_1^2\sigma^2_{\epsilon,t} I\big),$$ where ξ_t is the independent Gaussian component of the quantization noise. Our DNS derivation then starts from the corresponding quantized reverse conditional (Eq. 15), which folds the independent quantization noise into the reverse: $$p'_\theta(x_{t-1} \mid x_t) = q_\sigma\left(x_{t-1} \mid x_t, \hat{x}'_0\right) = \mathcal{N}\Big(x_{t-1}; \hat{\mu}_t(x_t, \hat{x}_0),\, (\sigma_t^2 + C_1^2\sigma^2_{\epsilon,t}) I\Big).$$ Thus the induced conditional marginal distribution under quantization is (Eq. 17): $$q'(x_{t-1} \mid x_0) = \mathcal{N}\Big(x_{t-1}; \sqrt{\bar{\alpha}_{t-1}}\, x_0,\, (1 - \bar{\alpha}_{t-1} + C_1^2\sigma^2_{\epsilon,t}) I\Big).$$ DNS then uses Eqs. 18–20 to construct a distributional map that identifies this quantized marginal with an unquantized marginal at a shifted time τ; in particular, Eq. 18 gives $$q'(x_{t-1} \mid x_0) \;\longleftrightarrow\; q\big(C_2 x_\tau \mid x_0\big),$$ and Eq. 20 defines the time shift τ and the corresponding time-shifted scheduler $\bar{\alpha}^{(q)}_{t-1} := \bar{\alpha}_\tau$, this explicitly constructs a distribution-preserving map that sends the quantized marginal to an original (unquantized) marginal at the shifted time τ.

Table 6. Concise comparison between DNS and prior work

Method	Parameter update?	Arch.changes or limits?	Integer-only Inference?	Plug-and-play over other PTQ?	Stoch.	Det.	FM
Q-Diffusion	Yes (Calibration, weight/quant update)	No	Yes	Not over SVDQuant	Yes	Yes	Yes
PTQ4DiT	Yes (Calibration, weight/quant update)	No Designed for DiT	Yes	Only DiT	Yes	Yes	Yes
SVDQuant	Yes (Weight update and FP16 finetune)	Add FP16 LoRA (Incomplete quant.)	No (Mixed Precision)	Not over many model-changing PTQ	Yes	Yes	Yes
PTQD	No	No	Yes	Almost Yes	Yes	No	No
DNS (Ours)	No	No	Yes	Almost Yes	Yes	Yes	Yes

A.3. Details of Flow-matching Derivation

In FLUX.1, the forward process is defined as:

$$\boldsymbol{x}_t = (1 - \sigma_t) \cdot \boldsymbol{x}_0 + \sigma_t \cdot \varepsilon \tag{42}$$

where $\varepsilon \sim \mathcal{N}(0, \mathbf{I})$ and σ_t represents the noise level at time t.

The denoising process follows a discrete update rule:

$$\boldsymbol{x}_{t_{next}} = \boldsymbol{x}_t + \Delta\sigma \cdot v_\theta(\boldsymbol{x}_t, \sigma_t) \tag{43}$$

where $\Delta\sigma = \sigma_{t_{next}} - \sigma_t$ and $v_\theta(\boldsymbol{x}_t, \sigma_t)$ is the velocity field predicted by the model.

When employing a quantized model, the velocity field prediction contains quantization-induced errors:

$$v'_\theta(\boldsymbol{x}_t, \sigma_t) = v_\theta(\boldsymbol{x}_t, \sigma_t) + \Delta v_\theta(\boldsymbol{x}_t, \sigma_t) \tag{44}$$

To ensure that this error approximates a Gaussian distribution, we apply transformation T:

$$T(v'_\theta(\boldsymbol{x}_t, \sigma_t)) = v_\theta(\boldsymbol{x}_t, \sigma_t) + \Delta' v_\theta(0, \sigma_{v,t}) \tag{45}$$

where $\Delta' v_\theta(0, \sigma_{v,t}) \sim \mathcal{N}(0, \sigma_{v,t}^2 \mathbf{I})$.

The denoising process with quantization errors becomes:

$$\begin{aligned} \boldsymbol{x}'_{t_{next}} &= \boldsymbol{x}_t + \Delta\sigma \cdot [v_\theta(\boldsymbol{x}_t, \sigma_t) + \Delta' v_\theta(0, \sigma_{v,t})] \\ &= \boldsymbol{x}_{t_{next}} + \Delta\sigma \cdot \Delta' v_\theta(0, \sigma_{v,t}) \end{aligned} \tag{46}$$

Substituting the forward process expression for $\boldsymbol{x}_t$:

$$\boldsymbol{x}'_{t_{next}} = (1 - \sigma_{t_{next}}) \cdot \boldsymbol{x}_0 + \sigma_{t_{next}} \cdot \varepsilon + \Delta\sigma \cdot \Delta' v_\theta(0, \sigma_{v,t}) \tag{47}$$

Drawing from our diffusion derivation, we seek a transformation that maps $\boldsymbol{x}'_{t_{next}}$ back to the standard forward path. We introduce a scaling factor C_2 and a new timestep τ that together establish an equivalence between the quantized output and a point on the original path. Specifically, we define:

$$C_2 \cdot \boldsymbol{x}_\tau = C_2 \cdot (1 - \sigma_\tau)\boldsymbol{x}_0 + C_2 \cdot \sigma_\tau \varepsilon' \tag{48}$$

Then we can establish that when $C_2 = (1 - \sigma_{t_{next}}) + \sqrt{\sigma_{t_{next}}^2 + \Delta\sigma^2 \sigma_{v,t}^2}$ and $\sigma_\tau = (C_2 + \sigma_{t_{next}} - 1)/C_2$, $\boldsymbol{x}'_{t_{next}}$ and $C_2 \boldsymbol{x}_\tau$ become statistically equivalent, with matching coefficients for $\boldsymbol{x}_0$ and equivalent variance terms for the noise components $\sigma_{t_{next}} \cdot \varepsilon + \Delta\sigma \cdot \Delta' v_\theta(0, \sigma_{v,t})$.

Importantly, neural networks trained for flow-matching are designed to estimate the velocity field pointing from any noisy sample toward the clean data. Since the network is trained to predict $v_\theta(\boldsymbol{x}_t, \sigma_t) \approx \mathbb{E}[\varepsilon | \boldsymbol{x}_t, \sigma_t]$ for any valid noise distribution, it can still function effectively when the noise distribution changes from ε to ε'. The model will naturally predict the velocity field that directs $\boldsymbol{x}_\tau$ toward $\boldsymbol{x}_0$, allowing our transformation to effectively absorb quantization errors.

A.4. Visualization Results

In this section, we demonstrate the visualisation results by different models. (1) LDM-4: Tested with 20 steps, guidance scale 3.0, and 256×256 resolution. We compare the FP16 model, Q-Diffusion (W4A8), its combination with PTQD and its combination with ours. The results are shown in Fig. 8. (2) DiT-XL: Evaluated with 20 steps, guidance scale 1.5, and 256×256 resolution. We compare the FP16 model, PTQ4DiT (W4A8), its combination with PTQD and its combination with ours. The results are shown in Fig. 9.

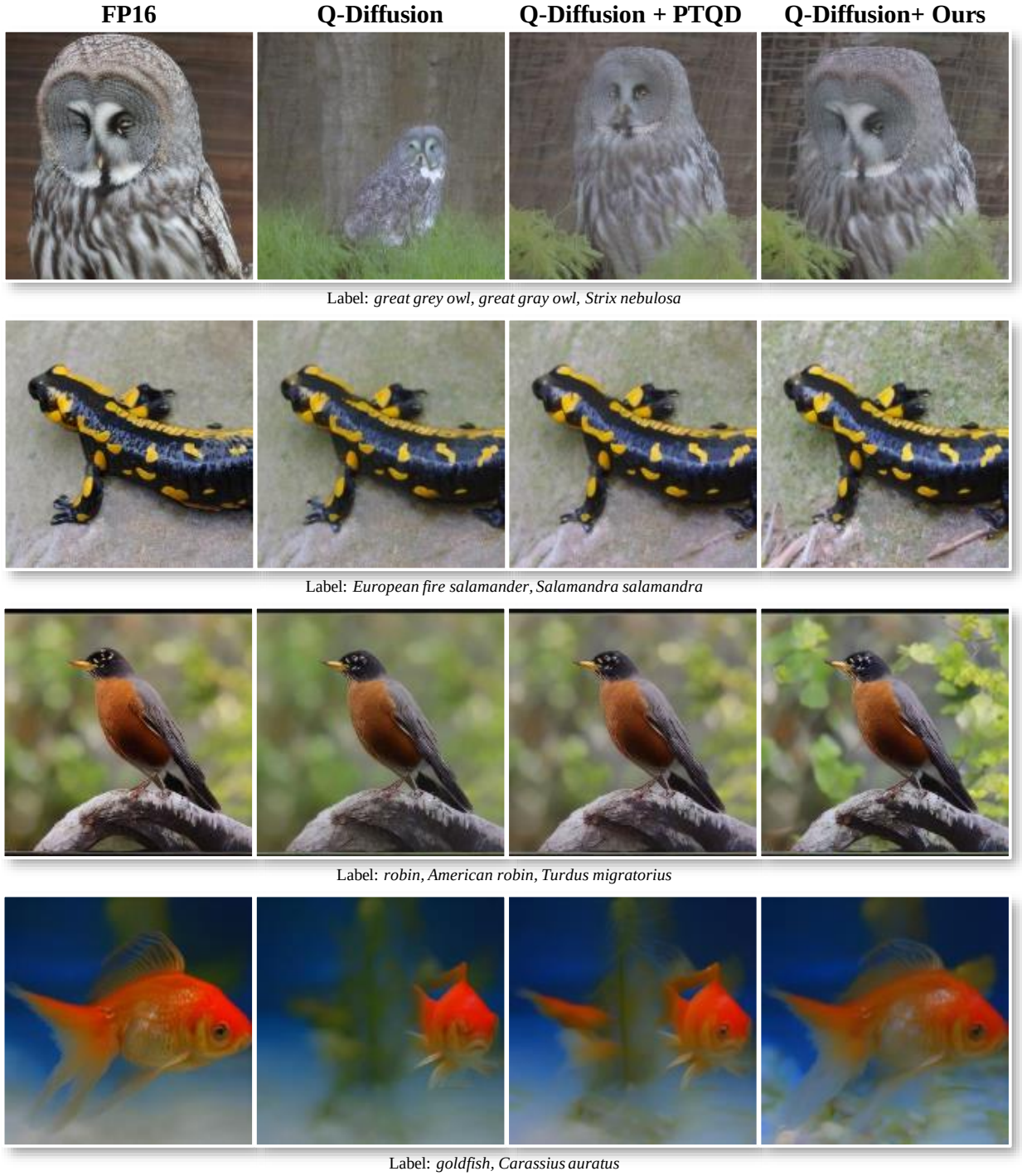

Figure 8. Tested the LDM-4 model with Q-Diffusion quantization to W4A8 precision. The resolution of the generated image is 256

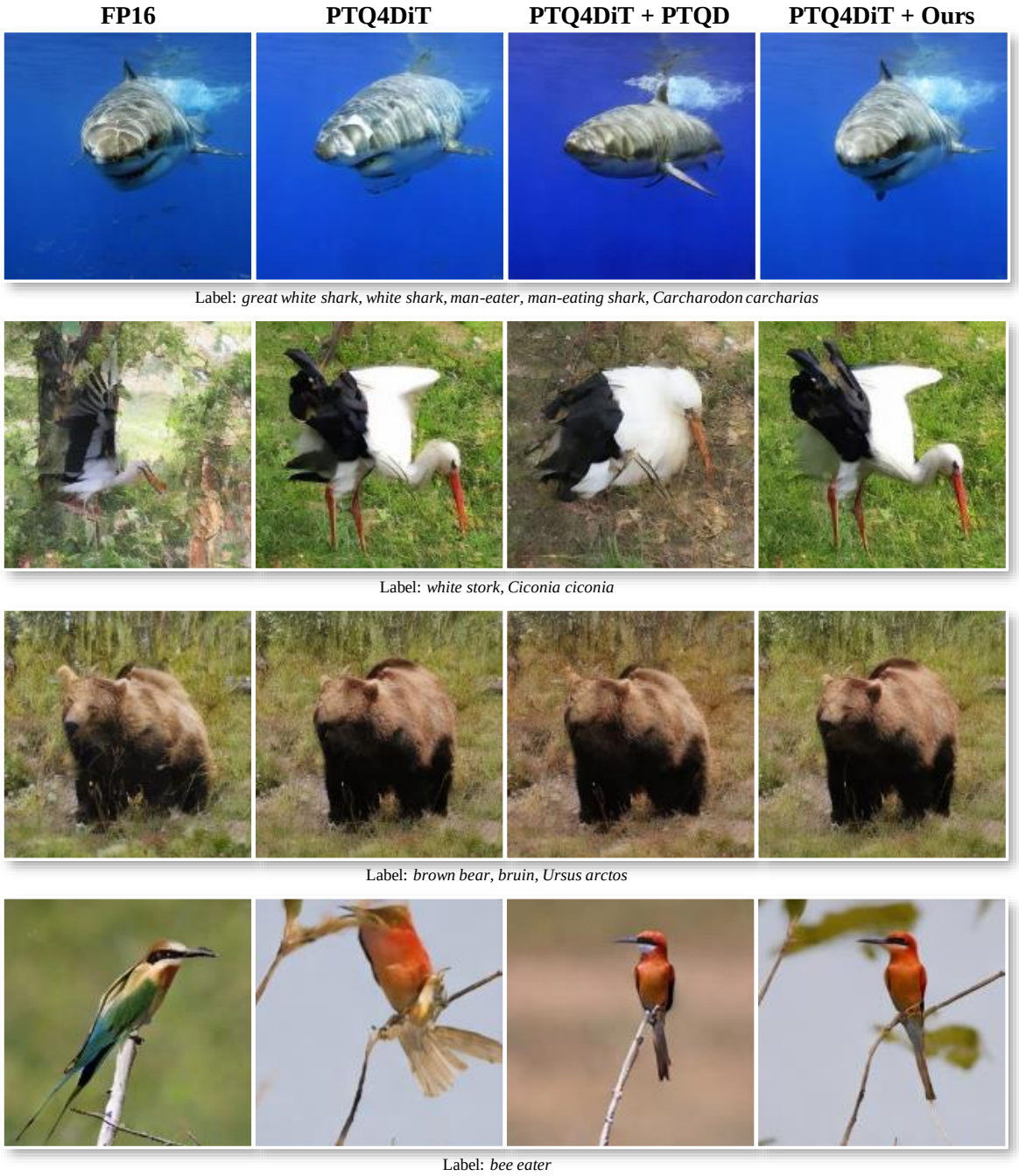

Figure 9. Tested the DIT-XL model with PTQ4DiT quantization to W4A8 precision. The resolution of the generated image is 256

(3) FLUX.1 : Tested with guidance scale 3.5, 20 steps at 256×256 and 1024×1024. We compare the FP16 model, SVDQuant (W4A4) with quantized its LoRA branch weight to 6-bit and its combination with ours. PTQD does not support Flow-matching. The results are shown in Fig. 10, Fig. 11, Fig. 12. Fig. 13 and Fig. 14. It can be seen that our method has good results in maintaining semantics, reducing artifacts, increasing details, and improving diversity, which shows that we have successfully achieved the goal of distribution preservation.

(4) FLUX.1 : We also try optimizing SVDQuant (W4A4) with FP16 LoRA branch. Tested with guidance scale 3.5, 20 steps at 256×256 and 1024×1024. We compare FP16 model, SVDQuant (W4A4) with FP16 LoRA and its combination with ours. The results are shown in Fig. 15 and Fig. 16. Our method still has capability to improve under strong baseline.

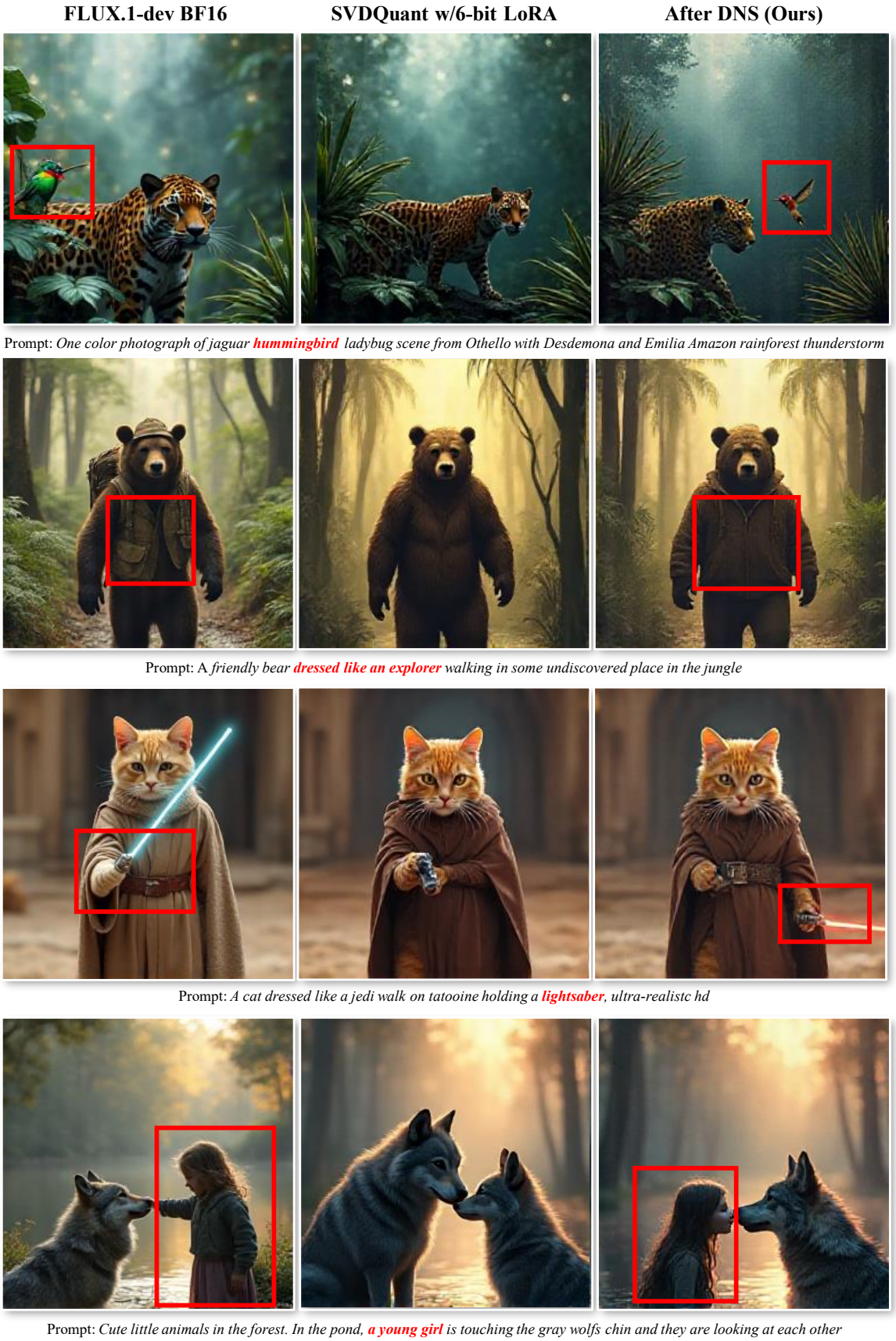

Figure 10. Tested the FLUX.1 model with SVDQuant quantization to W4A4 precision(also quantized SVDQuant LoRA branch weight to 6bit). The resolution of the generated image is 256

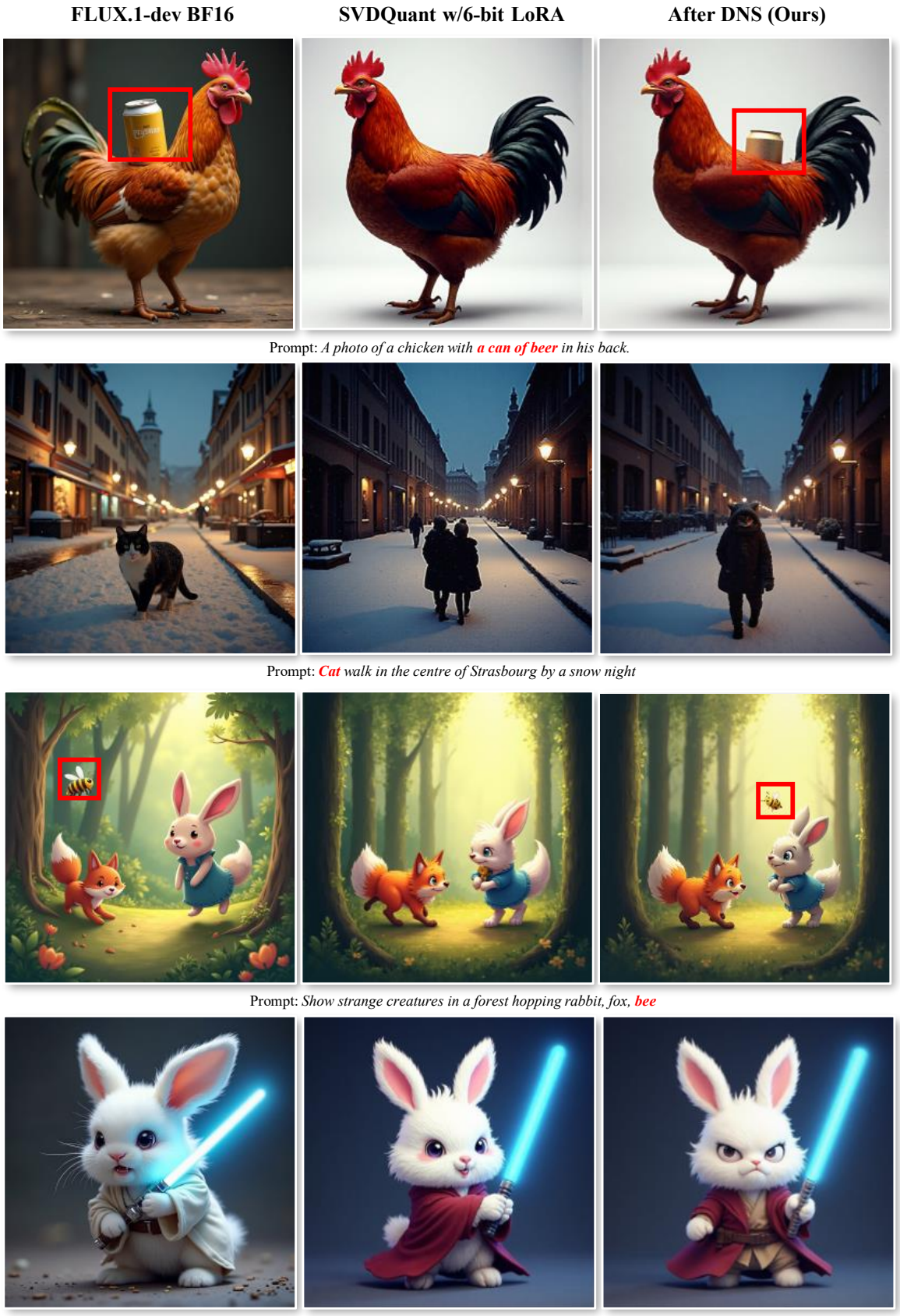

Figure 11. Tested the FLUX.1 model with SVDQuant quantization to W4A4 precision(also quantized SVDQuant LoRA branch weight to 6bit). The resolution of the generated image is 1024. It can be seen that we have successfully maintained and recovered some semantics.

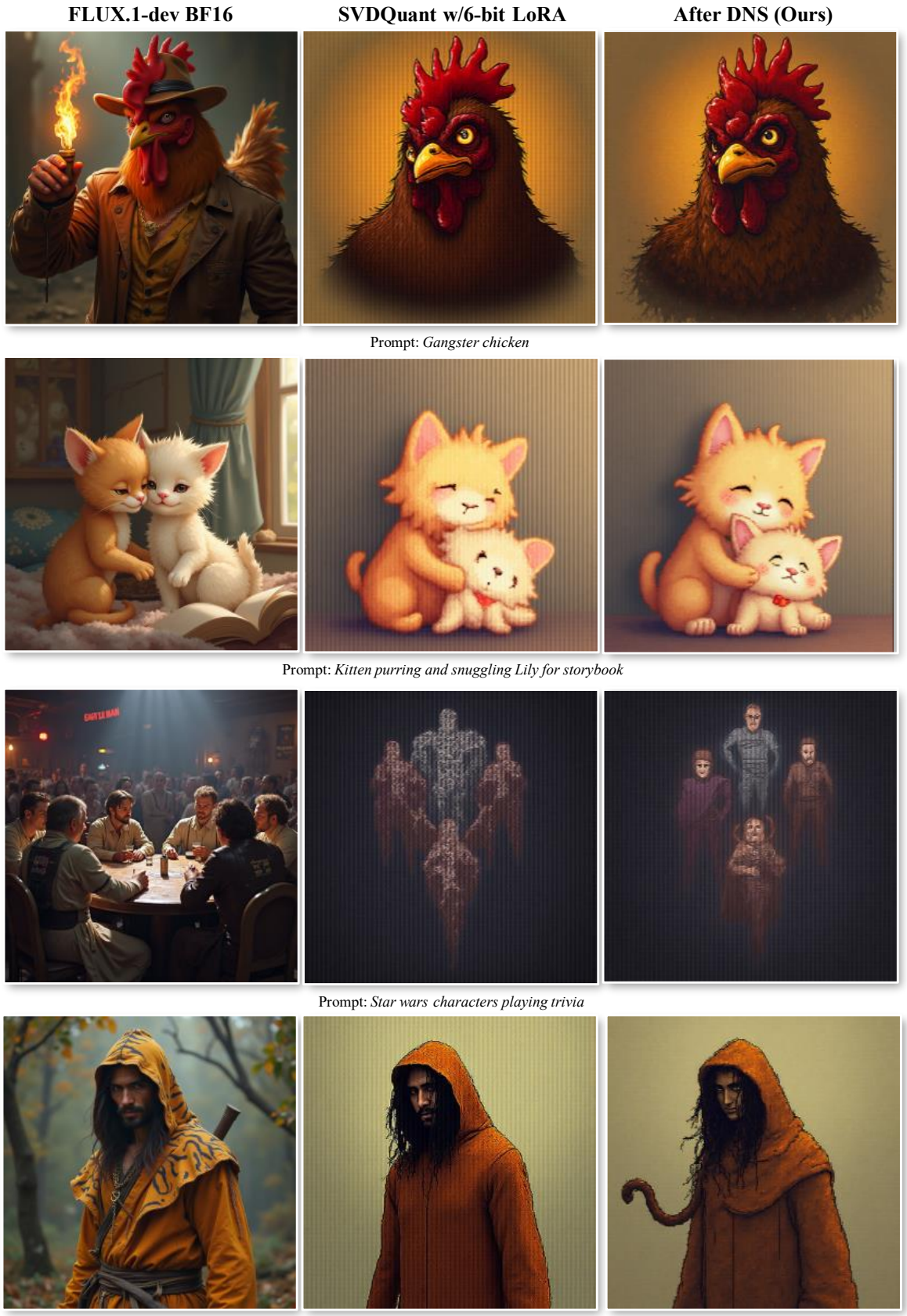

Figure 12. Tested the FLUX.1 model with SVDQuant quantization to W4A4 precision(also quantized SVDQuant LoRA branch weight to 6bit). The resolution of the generated image is 1024. It can be seen that we have successfully removed some artifacts, but the excessive artifacts introduced by quantization still cannot be completely removed.

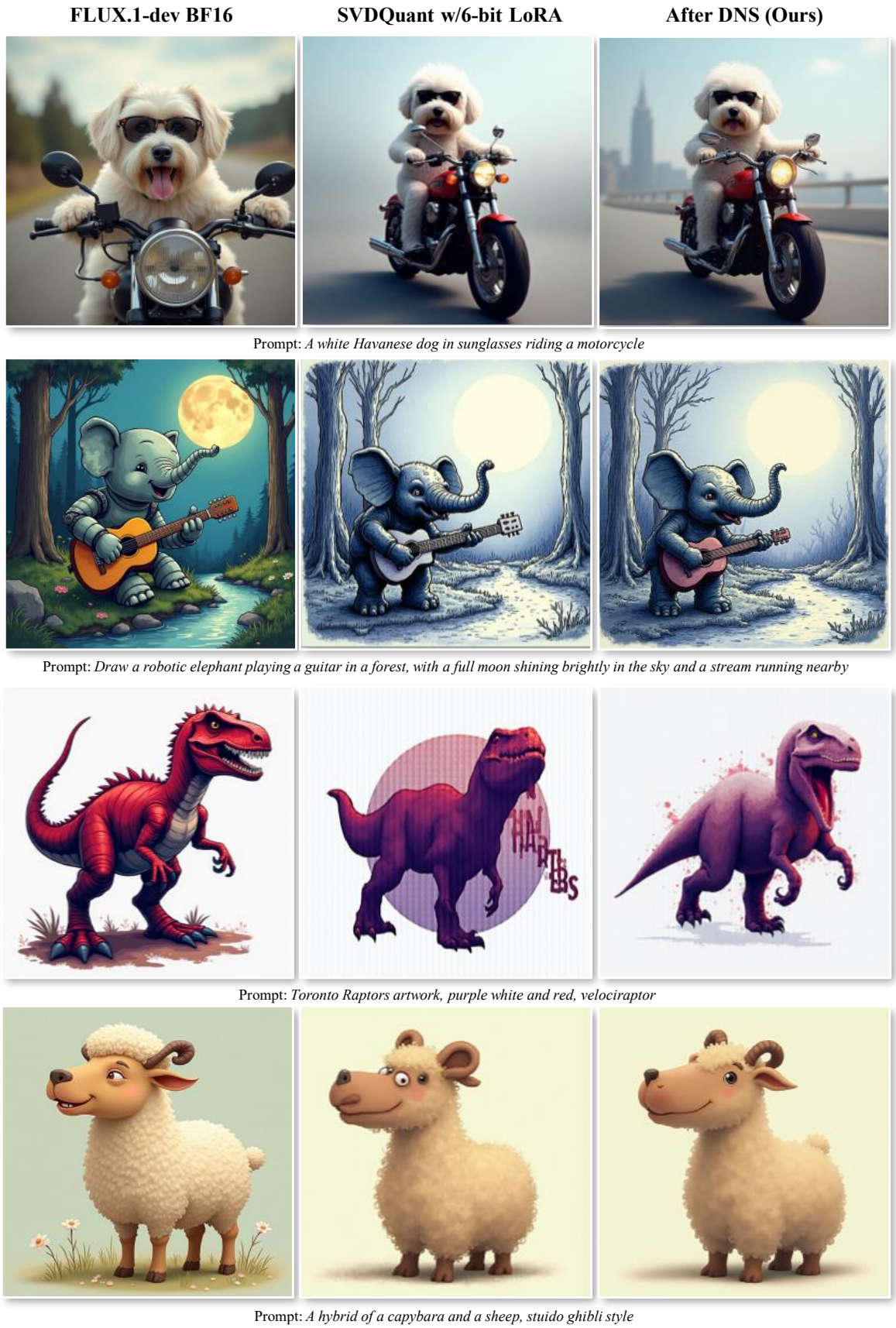

Figure 13. Tested the FLUX.1 model with SVDQuant quantization to W4A4 precision(also quantized SVDQuant LoRA branch weight to 6bit). The resolution of the generated image is 1024. It can be seen that we successfully added some details and improved the image quality.

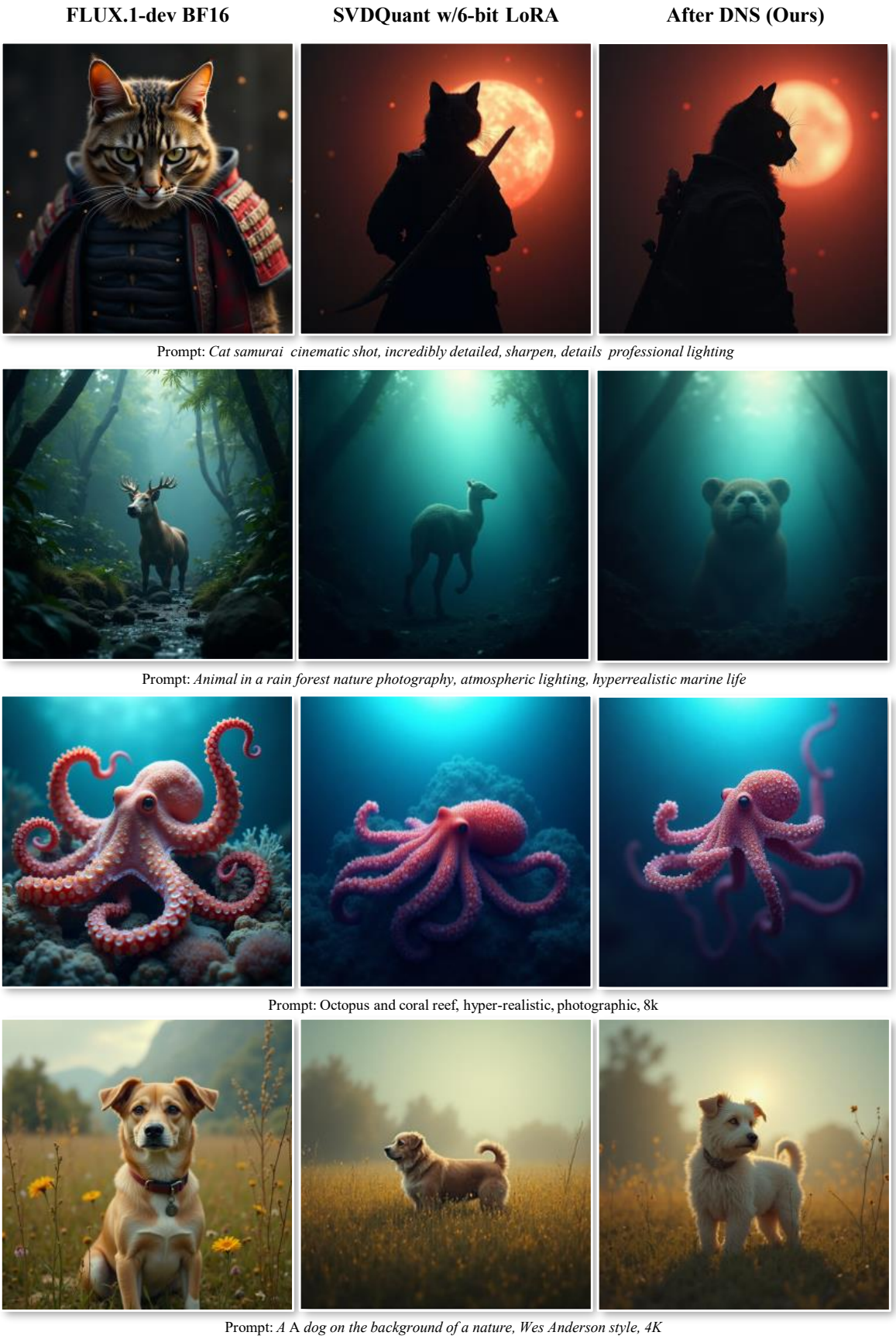

Figure 14. Tested the FLUX.1 model with SVDQuant quantization to W4A4 precision(also quantized SVDQuant LoRA branch weight to 6bit). The resolution of the generated image is 1024. It can be seen that since we are using distribution preservation, some images will also move to other trajectories with the same(as quantized model) quality.

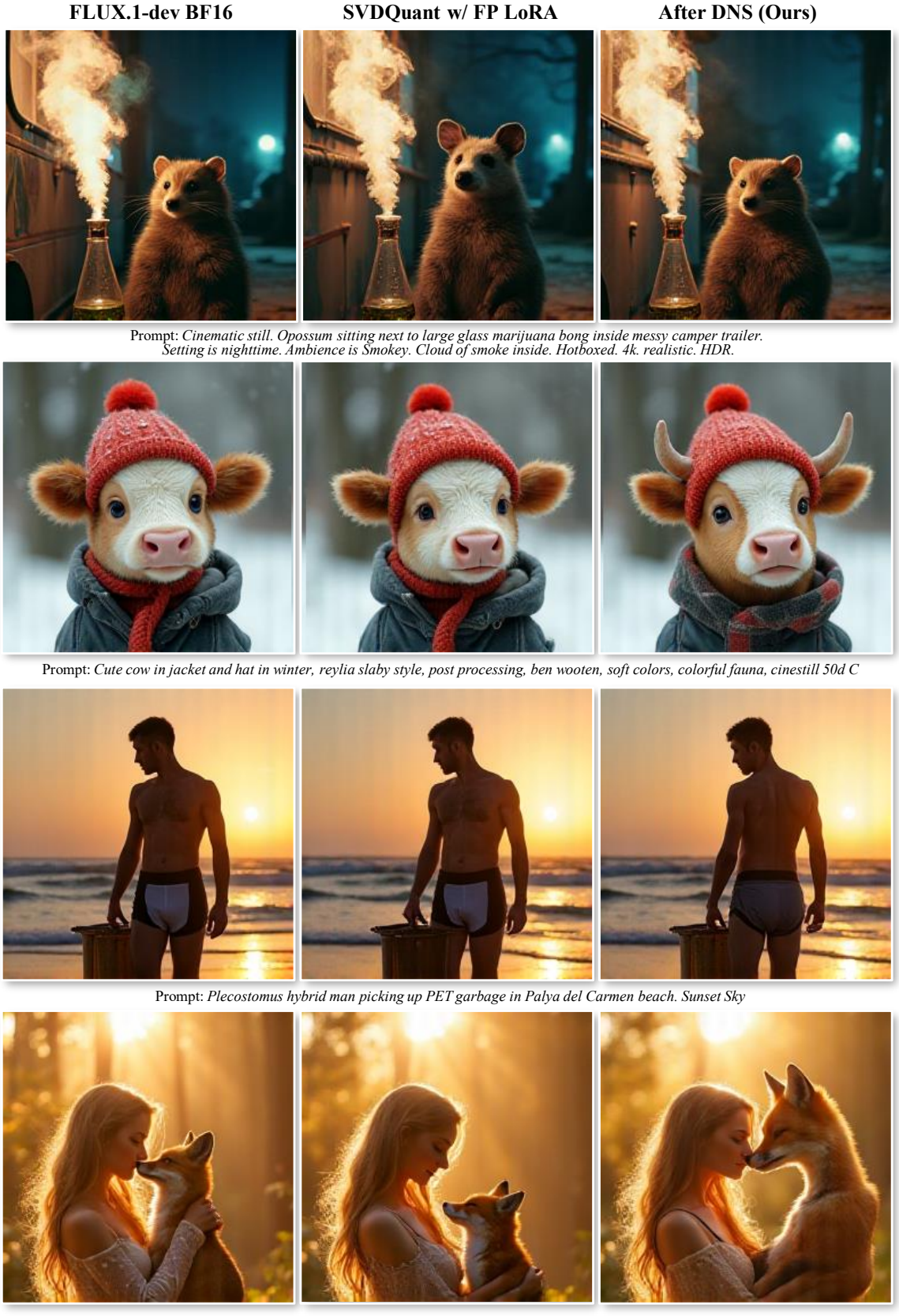

Figure 15. Tested the FLUX.1 model with SVDQuant quantization to W4A4 precision(maintain SVDQuant LoRA branch precision at W16A16). The resolution of the generated image is 256

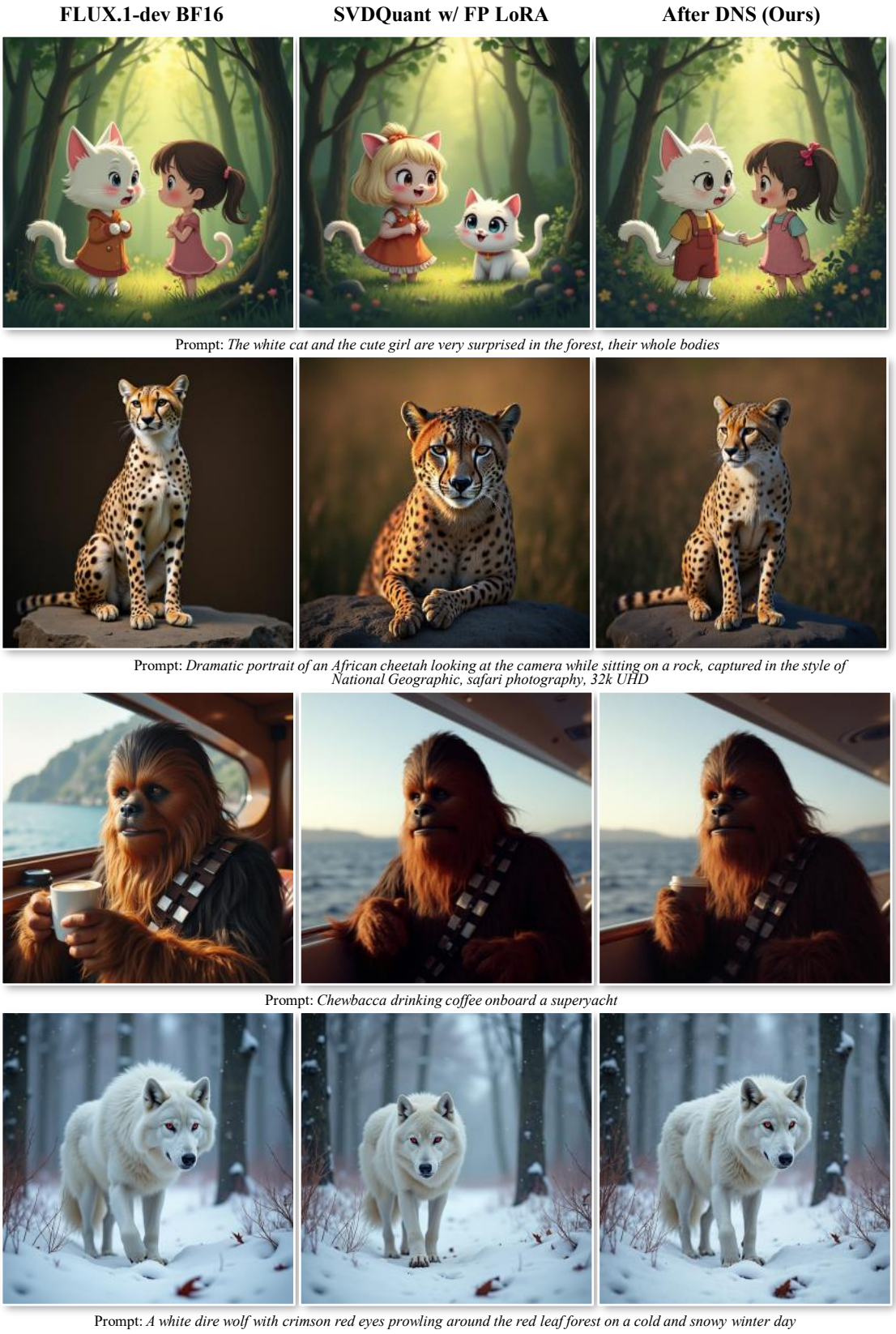

Figure 16. Tested the FLUX.1 model with SVDQuant quantization to W4A4 precision(maintain SVDQuant LoRA branch precision at W16A16). The resolution of the generated image is 1024

A.5. Additional Experiments Results

Ablation of Optimization Methods As shown in Tab. 8, we conduct a systematic ablation study to evaluate the contribution of each component in our framework. Starting from the W4A8 baseline quantized model (with Q-Diffusion) and applying CNC preprocessing, we progressively incorporate our proposed techniques to demonstrate their effectiveness. First, the DNS absorbs quantization noise through a timestep shift, adjusting the diffusion schedule to preserve the original denoising distribution. Second, the DCNC refines noise estimation by more accurately modeling the statistical properties of quantization errors.

Table 7. Performance comparison of different variance estimation methods

Model	Method	FID↓	IR↑	PSNR↑
LDM-4	-	9.85	0.012	23.09
	MAD	9.83	0.014	23.10
	IQR	9.81	0.015	23.10
	KUS	9.85	0.016	23.12
	KDE	9.83	0.012	23.10

Table 8. Effect of different components

Model	Method	FID↓	IR↑	PSNR↑
LDM-4	base	10.61	-0.01	22.81
	+CNC	10.32	-0.031	23.13
	+DNS	10.02	0.009	22.83
	+DCNC	9.81	0.015	23.10

Variance Estimation As shown in Tab. 7, we test five statistical methods for variance estimation: standard deviation, mean absolute deviation (MAD), interquartile range (IQR), kurtosis-based correction (KUS), and kernel density estimation (KDE). It can be seen that IQR demonstrates best performance on multiple metrics simultaneously.

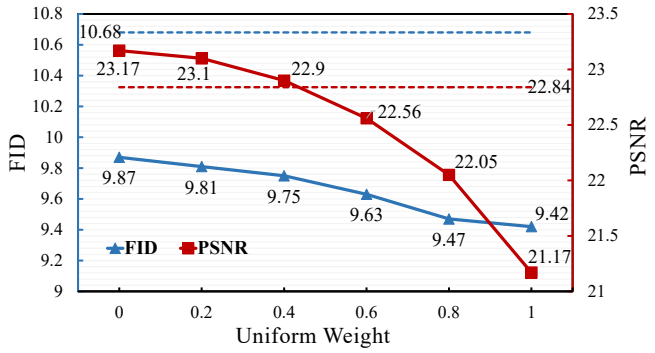

Figure 17. Performance comparison with different strength of correction

Uniform Weight Fig. 17 shows our experiments with different strength of correction (W_u) ranging from 0 to 1. We observed an interesting trade-off: higher W_u values improve generation quality (FID) but reduce similarity to full-precision outputs (PSNR). We select $W_u = 0.2$ for our experiments, as this value achieves a favorable balance between maintaining reasonable similarity while still improving the generation quality.

More Backbones Experiments In addition to the main backbones quantized with Q-Diffusion, PTQ4DiT, and SVDQuant, we further evaluate DNS on other PTQ methods: TFMQ-DM, PTQ4DM, and APQ-DM. We follow exactly the same evaluation protocol and metrics as in Sec. 5.1 and results are shown as Tab. 9-Tab. 11.

Table 9. CIFAR-10 (32×32) generation with TFMQ-DM (W4A8), 20 steps

Method	FID↓	sFID↓	KID×10^3 ↓	IS↑	PSNR↑	LPIPS↓
FP16	7.32	7.35	–	9.27	–	–
TFMQ-DM	12.83	15.69	3.59	9.26	27.81	0.138
w/ours	**11.12**	**13.03**	**2.20**	**9.50**	**28.66**	**0.120**

Table 10. Unconditional ImageNet-64 (64×64) generation with PTQ4DM(W8A8), 20 steps

Method	FID↓	sFID↓	KID×10^3 ↓	IS↑	PSNR↑	LPIPS↓
FP16	17.89	10.48	–	15.05	–	–
PTQ4DM	25.36	18.13	8.12	15.10	19.88	0.232
w/ours	**24.32**	**17.65**	**6.35**	14.69	19.71	0.241

Table 11. CIFAR-10 (32×32) generation with APQ-DM(W6A6), 20 steps

Method	FID↓	sFID↓	KID×10^3 ↓	IS↑	PSNR↑	LPIPS↓
FP16	11.32	8.88	–	8.50	–	–
APQ-DM	16.22	8.17	5.95	8.65	24.28	0.159
w/ours	**15.11**	**7.98**	**3.86**	8.56	**26.38**	**0.150**

Robustness and Statistical Reliability of Experiments To further assess the robustness and statistical reliability of our results, we report mean ± standard deviation of three evaluation metrics for representative backbones, as summarized in Tab. 12.

Table 12. Quantitative metrics with mean ± standard deviation.

Model	Method	FID↓	sFID↓	IS↑	PSNR↑
LDM-4	FP16	11.49 ± 0.009	9.99 ± 0.001	104.74 ± 0.020	–
	Q-Diffusion	10.68 ± 0.476	13.71 ± 1.998	101.95 ± 0.261	22.84 ± 0.269
	w/ours	9.81 ± 0.472	9.42 ± 0.126	102.40 ± 0.359	23.10 ± 0.438
CIFAR	FP16	7.32 ± 0.005	7.35 ± 0.003	9.27 ± 0.002	–
	TFMQ-DM	12.83 ± 0.002	15.69 ± 0.008	9.26 ± 0.006	27.81 ± 0.001
	w/ours	11.12 ± 0.042	13.03 ± 0.012	9.50 ± 0.006	28.66 ± 0.005
ImageNet64	FP16	17.89 ± 0.017	10.48 ± 0.005	15.05 ± 0.019	–
	PTQ4DM	25.36 ± 0.331	18.13 ± 0.132	15.10 ± 0.027	19.88 ± 0.214
	w/ours	24.32 ± 0.142	17.65 ± 0.170	14.69 ± 0.022	19.71 ± 0.212
CIFAR	FP16	11.32 ± 0.001	8.88 ± 0.003	8.50 ± 0.003	–
	APQ-DM	16.22 ± 0.400	8.17 ± 0.070	8.65 ± 0.003	24.28 ± 0.254
	w/ours	15.11 ± 0.160	7.98 ± 0.107	8.56 ± 0.001	26.38 ± 0.040

More Metrics In addition to FID, sFID, IS, IR, CLIP, and PSNR, we further evaluate Kernel Inception Distance (KID (Bińkowski et al., 2021)) and LPIPS (Zhang et al., 2018). KID is computed as the squared Maximum Mean Discrepancy between the feature distributions of real and generated images, using the same Inception-V3 backbone as our FID computation. LPIPS measures perceptual distance between image pairs based on deep features from a VGG network, with lower values indicating closer perceptual similarity.

Our primary goal is distribution preservation. Accordingly, FID and KID are especially important, as they quantify distances between feature distributions of generated and FP images under a pre-trained network. By contrast, LPIPS follows the same trend as PSNR: both are pixel- or patch-level similarity metrics that capture per-sample trajectory differences with respect to the FP model and therefore cannot directly validate whether the final outputs achieve better distribution preservation or overall generation quality at the distribution level.

The results, computed under the same settings as in our main experiments for each backbone, are shown in Tab. 13.

To further assess the generality of our approach, we combine it with three representative PTQ methods: TFMQ-DM on CIFAR-10, PTQ4DM on ImageNet-64, and APQ-DM on CIFAR-10. In all three settings, our method consistently improves the generative quality(including FID, KID, etc) over the corresponding PTQ baselines. Concretely, we observe reductions in FID about 4%-13%, in sFID about 2%-17% and in KID about 21%-38% across these experiments. These consistent improvements indicate that our method is effective at preserving distribution under multiple PTQ schemes, leading to quantized model distribution more closely match the FP model distribution.

Table 13. Additional experiments with KID and LPIPS across various backbones

Model	Bit	Method	KID$\times 10^3 \downarrow$	LPIPS$\downarrow$
LDM-4	W4A8	Q-Diffusion	4.56	0.205
		w/PTQD	3.89	0.206
		w/ours	3.01	0.220
DiT-XL	W4A8	PTQ4DiT	1.00	0.396
		w/PTQD	2.41	0.468
		w/ours	0.86	0.401
FLUX.1	W4A4 *w*/W16 LoRA	SVDQuant	0.08	0.197
		w/ours	0.08	0.214
	W4A4 *w*/W6 LoRA	SVDQuant	1.47	0.412
		w/ours	1.22	0.431
ImageNet64	W8A8	PTQ4DM	8.12	0.232
		w/ours	6.35	0.241
CIFAR-10	W4A8	TFMQ	3.59	0.138
		w/ours	2.20	0.120
	W6A6	APQ	5.95	0.159
		w/ours	3.86	0.150

Ablation under Other Backbone In addition to the LDM-4 analysis already presented, we have extended the ablations to the DiT-XL backbone with PTQ4DiT(Setup is the same as the main result: Using DiT-XL model with PTQ4DiT W4A8 quantization, step=20). We perform the same component-wise ablations as in Sec. 5.3: The results are shown in Tab. 14, Tab. 15, and Fig. 18.

As we can see in Tab. 14, IQR-based variance estimation again performs the best. And in Tab. 15, DNS and especially DCNC consistently improve over the PTQ base model, even for a large-scale backbone like DiT-XL. In Fig. 18, the performance remains stable across a wide range of W_u values, and the same qualitative behavior holds across different architectures and datasets. Specifically, FID fluctuates somewhat but remains much smaller than before DNS(ours). PSNR decreases slowly as W_u increases. This is consistent with our goal distribution-preserving. Based on these observations, we adopt a single fixed default of W_u=0.2 for all models, without any per-model or per-dataset tuning.

Table 14. Performance comparison of different variance estimation methods in PTQ4DiT.

Model	Method	FID$\downarrow$	IR$\uparrow$	PSNR$\uparrow$
DiT-XL	–	8.55	-0.486	17.33
	mad	8.56	-0.484	17.34
	iqr	8.51	-0.484	17.43
	kus	8.55	-0.487	17.39
	kde	8.56	-0.485	17.33

Table 15. Effect of different components in PTQ4DiT.

Model	Method	FID$\downarrow$	IR$\uparrow$	PSNR$\uparrow$
DiT-XL	base	9.83	-0.508	17.42
	+CNC	14.01	-0.609	16.32
	+DNS	9.78	-0.496	17.02
	+DCNC	8.51	-0.484	17.43

Ablation about More Parameters We also conducted additional experiments across various sampling steps (10, 20, 40) and guidance scales (0, 3.0, 6.0) and result is shown as Tab. 16.

Our supplementary experiments show that our method consistently maintains superior FID, sFID, IS, and IR scores across all tested configurations. The results demonstrate that our approach remains effective regardless of the number of DDIM steps or guidance scale settings, indicating robust performance across different inference schedules.

The bold part indicates that w/ours is better than other W4A8 indicators.

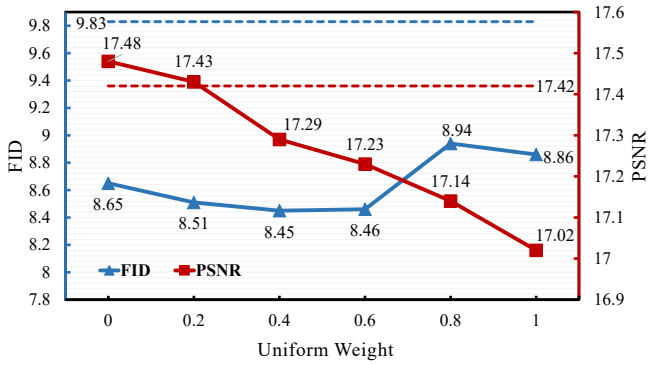

Figure 18. Performance comparison with different strength of correction in PTQ4DiT.

Table 16. Additional experiments across various sampling steps and guidance scales

LDM-4	Method	FID↓	sFID↓	IS↑	CLIP↑	IR↑	PSNR↑
scale=3.0 steps=20	FP16	11.49	9.99	104.74	31.91	0.134	—
	W4A8 Q-Diffusion	10.68	13.71	101.95	31.97	-0.014	22.84
	W4A8 w/PTQD	10.32	12.39	100.84	31.89	-0.031	23.13
	W4A8 w/ours	**9.81**	**9.42**	**102.40**	31.91	**0.015**	23.10
scale=3.0 steps=10	FP16	12.05	14.63	98.42	31.91	-0.095	—
	W4A8 Q-Diffusion	11.26	21.24	92.59	31.74	-0.298	24.88
	W4A8 w/PTQD	13.31	38.89	85.60	31.45	-0.467	20.74
	W4A8 w/ours	**10.43**	**14.94**	**93.29**	**31.76**	**-0.269**	**25.29**
scale=3.0 steps=40	FP16	10.66	9.15	106.32	31.81	0.215	—
	W4A8 Q-Diffusion	10.61	11.43	104.79	31.95	0.093	21.88
	W4A8 w/PTQD	10.85	10.92	102.12	31.87	-0.047	22.05
	W4A8 w/ours	**9.32**	**8.41**	104.75	31.83	**0.112**	21.89
scale=0.0 steps=20	FP16	51.94	10.99	21.91	20.01	-2.173	—
	W4A8 Q-Diffusion	59.95	20.32	20.52	20.32	-2.192	26.67
	W4A8 w/PTQD	58.64	20.34	20.12	20.47	-2.201	25.69
	W4A8 w/ours	**57.47**	**19.39**	**20.66**	20.30	**-2.168**	26.20
scale=6.0 steps=20	FP16	20.89	15.31	114.55	31.98	0.382	—
	W4A8 Q-Diffusion	20.18	15.77	114.34	32.16	0.289	19.55
	W4A8 w/PTQD	19.93	13.04	113.17	32.18	0.243	19.02
	W4A8 w/ours	**18.63**	**10.57**	**115.39**	**32.33**	**0.322**	19.22

Time and Memory Consumption Regarding our claims of "no extra steps" and "no additional memory", More details are shown in Tab. 17. At inference time, the only additional computation introduced by DNS+DCNC is applying the transformation $\mathcal{T}$ in Eq. 14 and using the pre-computed, timestep-dependent scalar coefficients(Algorithm 2). These operations reduce to elementwise additions and multiplications; we do not introduce any extra network forward passes, matrix multiplications, or large activation buffers.

On an A100-40G GPU, for LDM-4 + Q-Diffusion at 256×256 with 20 DDIM steps, generating 30,000 images, enabling DNS+DCNC incurs only 5.67 seconds of additional wall-clock time compared to PTQ alone. In comparison, generating 30k samples with the quantized model alone already takes about 5.1 hours on our setup, proving that increasing time of our method is almost negligible. The extra runtime buffers required by DNS+DCNC are about 320 KB, and the stored calibration parameters across all timesteps occupy less than 1 KB in total. For calibration, using 3000 images (as in our main experiments), computing the required statistics can be done once on CPU in about 214 seconds. Including both the FP16

and quantized forward passes needed to generate the calibration dataset, the entire calibration procedure takes approximately 45 mins on our setup (A100-40G GPU, LDM-4 + Q-Diffusion at 256×256 with 20 DDIM steps, sample 3000 images).

Table 17. Overview of calibration and inference overhead for our method (LDM-4 + Q-Diffusion).

Item	**Value**
Calibration (3,000 images, including FP16 + quantized)	45 min
Calibration statistics only (CPU, excluding sampling)	214 s
Sampling 30k images with quantized model	5.1 h
Extra time for 30k samples with DNS	5.67 s
Peak memory usage	1.5 GB
Additional memory overhead	320 KB